

Chapter 4

Detector Development: LSO Scintillator coupled to APD Arrays

4.1 Motivation

The in-beam positron emission tomograph BASTEI¹, under clinical operation since December 1997 at the German heavy ion tumor therapy facility at GSI Darmstadt [Eng04b], is based on the positron emission tomography (PET) technology for tracer imaging available at the time of installation. Consequently, its radiation detectors, scanner geometry and data acquisition and processing are suboptimal with respect to the requirements of next-generation, in-beam PET systems for therapy monitoring at future heavy ion clinics, namely high detection efficiency for annihilation radiation², a fast scintillator enabling the smallest time resolution for the suppression of random coincidences (chapter 6), good energy resolution for rejecting Compton photons scattered in the patient, insensitivity against influences from the therapy beam (chapter 5), hardness against hadronic radiation (chapter 5), magnetic field insensitivity, compactness and flexibility for positioning the patient at the beam delivery (chapter 3) and a fast signal processing and data acquisition able of separating the events acquired during the high rates registered during particle extractions (chapter 6).

The new scanner to be installed at the dedicated heavy ion facility in Heidelberg [Hea98] is to be operated close to the last beam bending magnet, which is not the case at the present fixed horizontal beam line in Darmstadt. For this reason, and because a reduction of the volume of the tomograph is highly desirable due to integration reasons³, the compact, magnetic field resistant avalanche photodiode arrays (APDA) become the detector of choice for scintillation readout, instead of the bulky, presently used photomultiplier tubes (PMT). In addition, the γ -ray detection material BGO is planned to be substituted with a state-of-the-art, commercially available scintillator that better satisfies the requisites mentioned. One possible candidate is cerium-doped lutetium oxyorthosilicate ($\text{Lu}_2\text{SiO}_5:\text{Ce}^{3+}$, LSO).

In the present chapter the physical and technological properties of the APDA scintillation detector, the LSO scintillator itself and the γ -ray detector resulting from the coupling of the two (LSO/APDA) are described, together with the optimization procedures endured before the construction of the detector. Finally, the imaging properties of two LSO/APDA detectors, assembled at the Forschungszentrum Rossendorf, are presented. The detectors are fully char-

¹ Beta activity measurements at the therapy with energetic ions.

² The presently installed scintillator, Bismuth Germanate ($\text{Bi}_4\text{Ge}_3\text{O}_{12}$, BGO), has a rather high intrinsic detection efficiency, therefore satisfying this requisite quite well.

³ This next-generation, in-beam PET must be accommodated in a cylindrical room with a diameter of 5 meters (chapter 3) together with the last beam bending magnet, the several detectors of the therapy-online-monitor system, the patient couch, the X-ray tubes and lasers for patient positioning verification and the mechanical structures holding all these devices.

acterized in single-mode operation and in coincidence with each other forming a very small positron tomograph.

4.2 Detection of γ -rays in Nuclear Medicine Imaging

Radiolabeled nuclear imaging techniques include high resolution ($< 100 \mu\text{m}$) *ex vivo* and *in vitro* autoradiographic techniques using film, phosphor storage plates or real time autoradiographic systems [Cha98], and *in vivo* methods using radionuclides that produce photons of appropriate energy (γ -rays, annihilation photons or characteristic X-rays with energies in the range of 25-511 keV) during decay [Che04b]. The *in vivo* methods are further divided into single photon imaging, utilizing radionuclides with single or multiple, uncorrelated γ -ray emissions detected by gamma camera¹ systems [Sho84] and PET, where β^+ -decaying radionuclides emit an energetic positron that annihilates into two, almost back-to-back 511 keV γ -rays after the positron thermalizes in the surrounding medium and annihilates itself with an atomic electron. A non-complete collinearity of the γ -rays emitted takes place and was measured to be $\leq 0.5^\circ$ FWHM² in water. It arises due to the momenta of both the thermalized positron and the atomic electron at the moment of annihilation [Phe75]. Because of this almost back-to-back photon emission and detection in a PET system, called electronic collimation, no physical collimation is required and, therefore, its sensitivity is much higher ($10^2 - 10^3$) than in a SPECT system. However, single-photon emitting radionuclides are generally more readily available than positron-emitting nuclides, as many of the latter have short half-lives [Che04b].

With a photon energy of 511 keV in PET, and a photon-energy range typically ≤ 400 keV in single-photon imaging, with the 140 keV γ -ray from ^{99m}Tc used most frequently [vE02], an efficient detection must rely on a conversion medium in which the incident γ -rays have a reasonable probability of interacting (section 4.2.1) and on a detector to read the output of the conversion medium (section 4.2.2).

4.2.1 Scintillators for γ -ray conversion

Ionization detectors that use a gas as the sensitive volume are poor detectors for counting both γ -rays and X-rays because of their low interaction probability and their weak capability to measure the energies of individual photons. Therefore, scintillator materials used in nuclear medicine are generally either inorganic substances in the form of solid crystals or organic substances both dissolved in liquid solution or dissolved in a solvent subsequently polymerized, i.e. forming a solid solution. Inorganic scintillators are employed in most of the current medical diagnostic imaging modalities using X-rays or γ -rays [Web90]. This is explained by the comparatively good detection efficiency of inorganic scintillators for hard radiation in respect to organic scintillators or solid detectors, i.e. silicon or germanium-based semiconductor detectors exposed directly to the photons.

Table 4.1 shows the main properties of the most important scintillators used, or under study and development, for γ -ray detection in radionuclide medical imaging. Its compilation was based mostly upon [vE02] and [Paw95], with information also from the references given in the Table and from [Cry00, Gro98a, Kno89]. The scintillator density ρ is multiplied by the fourth power of its effective atomic number Z_{eff} since the absorption by photoelectric effect per unit length is proportional to ρZ_{eff}^{3-4} [vE02]. For 511 keV quanta the chance of photoelectric effect at $Z = 80$ is less than 50 %, the other 50 % being the Compton effect, proportional to ρ . Depending

¹ If the gamma camera is rotated around the patient and used with tomographic acquisition and reconstruction techniques, the term SPECT (single photon emission computed tomography) arises.

² Full width at half maximum.

Table 4.1: Scintillators for γ -ray detection in radionuclide medical imaging.

Scintillator	Density ρ (g cm^{-3})	ρZ_{eff}^4 ($\times 10^6$ g cm^{-3})	Atten. length ^a (mm)	Photo effect fr. ^a (%)	Hygro- scopic	Yield (ph./ keV)	Decay const. (ns)	Peak emission (nm)	$\Delta E/E^b$ (%) FWHM	dE/dx per mip ^c (MeV/cm)	After- glow (%/ms)	Medical application	Reference(s)
NaI:Tl	3.67	24.5	29.1	17	Yes	41	230	410	5.6	4.8	0.3-5/6	SPECT	[Hof48, Sho84]
CsI:Na	4.51	38	22.9	21	Yes	40	630	420	7.4	5.6	0.5-5/6	XII	[He100]
CsI:Tl	4.51	38	22.9	21	Slightly	66	> 800 ^d	420	6.6	5.6	0.5-5/6	SPECT, PET, CT	[vE02, Gar00]
CsF	4.64	37	20.0	23	Very	2	3	390	4.3 ^e	6.0 ^g		TOF-PET	[Mos83]
BaF ₂	4.89	42	20.5	17	Slightly	2 ^f	0.7 ^f	220 ^f	10	6.6		TOF-PET	[Lav83]
BGO (Bi ₄ Ge ₃ O ₁₂)	7.13	227	10.1	40	No	9	300	480	9.0	9.2	0.005/3	PET	[Web73]
LSO (Lu ₂ SiO ₅ :Ce)	7.4	143	11.4	32	No	26	40	420	7.9	9.7 ^g	< 0.1/6	PET	[Mel92, Mel91]
LYSO $\frac{\text{Lu}}{\text{Y}}$ (Lu _{1.8} Y _{0.2} SiO ₅ :Ce) $\frac{90}{10}$	7.1	127	11.5		No	26 ^h	41	420	7-9	7.8 ^g	< 0.1/6	PET	[Coo00, Pid03]
(LuYSiO ₅ :Ce) $\frac{50}{50}$	6.0	75	16.7	21	No	26 ^h		420	7-9	7.1 ^g	< 0.1/6	PET	[Kim02, Mos99b]
LuAP (LuAlO ₃ :Ce)	8.3	148	10.5	30	No	12	18	365	~ 15	11.0 ^g		PET	[Min94, Mos95]
LPS (Lu ₂ Si ₂ O ₇ :Ce)	6.2	103	14.1	29	No	30	30	380	~ 10	8.3 ^g		DOI-PET	[Pau00]
LGSO (Lu _{0.4} Gd _{1.6} SiO ₅ :Ce)	6.5	79	14.3	26	No	16	65	440	8	8.6 ^g		PET	[Shi04]
GSO (Gd ₂ SiO ₅ :Ce)	6.7	84	14.1	25	No	8	60	440	7.8	8.7 ^g		PET	[Tak83, vE02]
YAP (YAlO ₃)	5.5	7	21.3	4.2	No	21	30	350	4.3	7.8 ^g		SPECT	[vL00]
LaCl ₃ :Ce	3.86	23.2	27.8	14	Yes	46	25 (65%)	353	3.3	5.2 ^g		SPECT	[vL01]
LaBr ₃ :Ce	5.3	25.6	21.3	13	Yes	61	35 (90%)	358	2.9	6.9 ^g		SPECT	[Sha04]
CeBr ₃	5.2	26.6	21.5	14	Yes	68	17	370	3.4	5.9 ^g		TOF-PET	[Sha04]
LXe (liquid xenon)	3.06	26	30.4	21	-	11	27 (30%)	165	22/16 ⁱ	3.9 ^g		DOI-PET	[Che83]
PbWO ₄	8.2	268	8.9	43	No	0.2	15	440-500		13.0			[Sch92, Cry00]
Plastic (vinyltoluene)	1.03	< 0.005	444	-	No	< 12	1-3	375-435	-				[Paw95, Bhr64]
Ideal (PET, PMT)	> 6	> 245	< 12	> 30	No	> 8	< 500	300-500	< 10	-			[Der82, Mos00]
Ideal (PET, APD)						≥ 8		400-900					
Ideal (TOF-PET)						≥ 8	< 40						

^a At 511 keV.^b At 662 keV, PMT readout.^c Minimum ionizing particle.^d Smaller than 6 μ s.^e At 662 keV, PMT and silicon drift detector (SDD) readout.^f Fast decay component.^g Extrapolation from $Z_{eff}/A \times \rho$, based on NaI.^h PMT readout, 33 ph./keV with APD readout.ⁱ At 511 keV, with 22% in [Che04a], 16% in [Cre00] (ionization mode).^j Arises from e^-/ion^+ recombination, vanishes under electric field.^s Slow decay component.

SPECT: Single photon emission computed tomography.

XII: X-ray image intensifier.

TOF-PET: PET with time-of-flight information.

DOI-PET: PET with depth-of-interaction information.

on the kind of scintillator and on the crystal size, detection of both the Compton electron and the Compton-scattered photon in the same crystal or detector may significantly contribute to the intensity of the full-energy peak, as demonstrated for example in positron emission mammography (PEM) dedicated systems using LSO scintillators coupled to APDA [San04]. In PET applications a scintillator with small attenuation length is necessary in order to minimize the crystal radial length, typically on the order of three times the attenuation length. This, in turn, minimizes the parallax error responsible for radial degradation of the images at voxels away from the isocenter of the tomograph [Hum03]. The photoeffect fraction, together with the photopeak energy resolution, are indeed important for a high full-energy peak intensity and, consequently, for a high detection efficiency of events valid for reconstruction, a low contribution of photons Compton-scattered in the patient, that show up as a continuous blur in the images, and a high true-to-random coincidence ratio since random events are more affected by Compton photons than true events [Mue02]. The photon yield and the decay constant of the scintillator play their role in minimizing the coincidence-time resolution $2 \Delta t$ achievable by the system. A small time resolution is mandatory for achieving the lowest random coincidence rate C_r possible since $C_r = 2 \Delta t C_i C_j$, where C_i and C_j are the singles count rates in detectors i and j forming the line of response (LOR) ij . Furthermore, a small scintillation decay time is also necessary for minimizing dead time, i.e. the time in which a coincidence cannot be registered because the PET system is busy handling a previous coincident event. Several parts of the system contribute to the dead time and the detector is one of them. Besides its influence on energy resolution, a high light yield is also important for achieving optimum spatial resolution at the detector in systems using scintillation-light sharing methods to reduce the number of readout electronic channels [Cas86, dG94, Wie94].

Additional prerequisites for an in-beam PET scintillator

In addition to the main scintillator properties described in the previous paragraph for nuclear medicine imaging with PET, the requirements of in-beam PET include also a radiation hard crystal that does not become activated, leading to γ -ray lines in the 511 keV region (experimental results in chapter 5). This is necessary due to the light particle flux consisting mainly of neutrons and protons, but also with slightly heavier particles, that has been measured to leave the irradiated patient downbeam, peaked in the forward direction [Gun04a, Gun04b].

All crystal scintillators suffer from radiation damage [Zhu98] when exposed to large radiation doses. The most common damage phenomenon is the appearance of radiation-induced absorption bands caused by color center formation. The absorption bands reduce the light attenuation length of the crystals and, consequently, its light output. Other effects include an increase in phosphorescence (afterglow), which leads to an increase in readout noise, and a reduced intrinsic scintillation light yield due to damage of the scintillation mechanism. Damage may recover both under room temperature, leading to a dose rate dependence [Zhu97], as well as after thermal annealing or optical bleaching¹. The effects usually can only be observed clearly in thick (> 5 cm) crystals [Bob84] and are dependent on the type of radiation [Kob83]. A material is usually called radiation hard if no measurable effects occur at a dose of 10 kGy. Examples of radiation hard materials are CdWO_4 , GSO and BaF_2 [Maj85]. In general, doped alkali halide scintillators such as NaI:Tl and CsI:Tl are rather susceptible to radiation damage, with NaI:Tl recovering the damage non spontaneously and CsI:Tl suffering permanent damage [Bob84].

The radiation resistance of scintillators commonly used in PET, like BGO and LSO, have been

¹ Thermal annealing and optical bleaching consist in applying a heat treatment ($\sim 500^\circ\text{C}$) or exposure to light in the visible/ultra-violet spectrum ($\sim 1\text{ mW/cm}^{-2}$), respectively, to the damaged crystal in order to rearrange its constituent atoms and crystal defects to a configuration similar to that existing before the irradiation, thus restoring to some degree its light transmission properties.

measured both for low-energy γ -rays, high-energy protons and fast neutrons for BGO [Kob83], as well as for X-ray exposure for LSO [Coo99]. For BGO, the studies with hadrons show a conservative value of 150 Gy as the maximum dose before 1% transmittance is lost after 20 radiation lengths. Furthermore, long lived excited states are produced in the crystal after a hadron dose of 10 kGy only, with disintegration rates of $10^2 \text{ s}^{-1} \text{ g}^{-1}$ and $35 \text{ s}^{-1} \text{ g}^{-1}$ corresponding to γ -ray lines above 500 keV and 1 MeV, respectively. In the case of pure LSO, an increase in absorbance of scintillating light of $\sim 10\%$ and 37% at 400 nm was measured after an exposure of 1 minute and 30 minutes, respectively, to an X-ray dose rate of 120 Gy min^{-1} . This behaviour was attributed to the enhancement of oxygen related defects and was not observed in cerium-doped LSO due to its activator-based scintillation mechanism [Kno89]. Cerium doped LSO is a fairly radiation hard scintillator up to 100 kGy [Mos02].

Scintillators commonly used in nuclear medicine

By far the most commonly used scintillator for nuclear medicine applications is the thallium-activated sodium iodide crystal NaI:Tl, used in combination with a PMT readout (section 4.2.2) mostly in single-photon emission systems but also in high resolution PET scanners [Ada01]. Other scintillators most suitable for PET at the current time are BGO, LSO, LuAP, LPS, GSO and YAP (Table 4.1). The most widely used in commercial PET scanners is BGO. It presents a high detection efficiency for 511 keV photons (a 3 cm long crystal has almost 3 attenuation lengths) and high photoeffect fraction, together with a relatively low production cost. The main disadvantages of BGO are its rather long decay time of 300 ns and low light yield in respect to other scintillators such as LSO, leading to worse time and energy resolutions, respectively. One of the most suitable scintillator material for PET is LSO. It presents a high ρZ_{eff}^4 , a high light yield, short decay time and relatively good mechanical properties necessary for high-throughput manufacturing. Due to its short decay constant a time resolution of 1.2 ns has already been achieved in a commercial PET scanner [Con03], with BGO-based tomographs presenting typically 12 ns. Therefore, renewed interest in profiting from the time-of-flight information in LSO-based tomographs has arisen [Mos04], with a commercial solution already on the market [Con03]. As mentioned before in this section, a commercial PEM system based on LSO scintillators coupled to APDA is under construction [San04]. Due to a scintillation readout on both sides of the LSO crystals, this system, expected to provide a time resolution of the order of 500 ps FWHM, will allow DOI-PET to be implemented in mammography applications. For completeness, it must be stated that several groups have been actively developing new PET methods and techniques using noble elements, like liquid xenon (LXe), in scintillation and ionization correlated modes [Cre00] in order to solve the problem of parallax error in PET [Che83, Col00].

4.2.2 Detectors for scintillation light collection

Current commercial PET scanners generally use detector modules readout in Anger logic, i.e. one scintillator detector block is implemented with saw cuts defining *individual* pixels and the scintillation light is read by several PMT [Mos94]. The analog ratios among the PMT signals yields the coordinate of the hit crystal [Ang58]. This reduces the number of electronic readout channels by a factor given by the ratio between the number of individual crystals and PMT but, on the other hand, increases the detector dead-time per front area unit¹ by the same amount and introduces a spatial resolution degradation of typically 2 mm added in quadrature to other factors influencing the spatial resolution of the tomograph [Mos93]. The reasons for using PMT for scintillation light readout are their much higher gain and better noise characteristics

¹ The detector dead-time per unit area is a figure of merit commonly used to describe the effective detector dead-time due to the scintillator decay time together with the readout scheme implemented [Mos94].

in respect to other more compact light detectors such as silicon-based APDA [Pic04]. Other photodetectors providing sufficiently high gain bandwidth for use in PET applications are multi-anode PMT [Suz93], metal channel dynode PMT [Kyu94], hybrid PMT¹ [Dat97], micro channel plate PMT (MCP-PMT) [Fie03], visible light photon counters² (VLPC) [Pet89] and Geiger-mode APD³ [Buh03]. The latter has been gaining increasing importance due to its low-cost, compactness, room-temperature operation capability, insensibility to magnetic field and hadrons and good timing characteristics in low-light environments, with pixel recovery times of about 20 ns. However, due to current fabrication limitations, the light pulses readout by Geiger-APD must be limited to 2×10^3 photons per mm^2 , which is still a too low dynamic range for PET applications. Multi-anode PMT, such as the 8×8 pixel, flat-panel PMT H8500 from Hamamatsu [Fie03], as well as MCP-PMT, such as the 8×8 pixel 85011-501 from Burle [Fie03], have recently made substantial progress towards delivering devices with high packing fractions of 90 and 70 %, respectively, high gain of 10^6 , excellent single-photon timing characteristics of 300 and 130 ps FWHM, respectively, and acceptable pixel-to-pixel uniformity with efficiency drops of 10-20 % at the edges. However, their quantum efficiencies lie below that of normal PMT by 20 and 30 %, respectively. Finally, multi-anode PMT cannot be used under magnetic fields, whereas MCP-PMT offer high magnetic field insensitivity.

Additional prerequisites for an in-beam PET detector

From the list of detector characteristics outlined in the previous paragraph, two must be underlined for a detector suitable for the next-generation in-beam PET: compactness and magnetic field insensitivity; and other two must be added for solid state detectors: radiation hardness and small nuclear counter effect⁴.

As detailed in chapter 3, this next-generation tomograph will have to adapt itself into different measuring positions in respect to the patient and patient-couch, the X-ray and laser patient positioning system, the detectors of the therapy on-line monitor and to the last portion of the rotating beam line (nozzle). This fact justifies efforts on reducing detector volume and, therefore, on the need for detector compactness. Concerning magnetic field insensitivity, Fig. 4.1 shows the calculated fringe magnetic field after the last beam bending magnet of the rotating gantry (nozzle). Depending on the irradiation portal selected, each PET detector will have to be positioned at different places in respect to the last magnet and, therefore, will have to operate under different magnetic field intensity and orientation from measurement to measurement. Furthermore, the magnetic induction is changing during the irradiation due to the variation of beam energy. This poses strong restrictions on the use of PMT, even with mu-metal shielding, since a decrease in gain between 10 and 15 % was measured with a magnetic field intensity of 2 mT only (20 Gauss) when the magnetic field was oriented along the longitudinal axis of the PMT [Bou00]. This decrease was measured with the ETL 9126FLB17 PMT, a linear focus dynode structure PMT with 11 amplification stages, and the PMT was covered with a mu-metal sheet extended to 30 mm beyond the photocathode. If the mu-metal sheet screening finished at the edge of the photocathode a decrease in gain of 50 % was already observed at a field intensity of 1 mT (10 Gauss). In addition to these facts, the park position of the PET scanner lies in close proximity to the last beam magnet. This may induce permanent malfunctioning or performance degradation onto the detectors. For these reasons, a magnetic field insensitive

¹ Also named hybrid photodiode or hybrid PD.

² Typically operated at liquid helium temperatures: 6.5 K.

³ Also named silicon photomultiplier (SiPM) or Geiger photodiode (GPD).

⁴ The nuclear counter effect is a quantification of the electrical signal generated by the passage of ionizing radiation through an APD. It is expressed as the effective thickness of a diode with gain 1 that generates the same signal as the APD under evaluation.

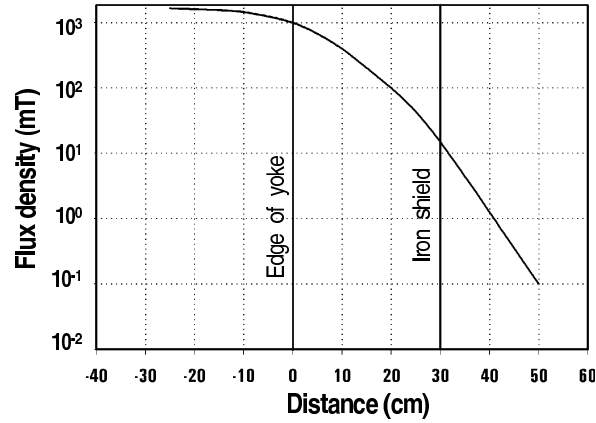


Figure 4.1: Calculated fringe magnetic field after the last beam bending magnet [Hab01].

device is the optimum detector for the next-generation in-beam tomograph.

In what concerns radiation hardness and small nuclear counter effect, these are needed due to the light particle flux that was measured to leave the patient downbeam [Gun04a, Gun04b]. Although the flux is mainly forwardly peaked and no detectors are expected to be positioned within an angle of $\pm 20^\circ$ in respect to the beam direction along the isocenter (chapter 3), the irradiation of large fields does bring the forwardly peaked light-particle flux in close proximity to the PET detectors. Therefore, radiation hard detectors with small nuclear counter effect are desirable.

Semiconductor photodetectors with internal amplification

The photograph in Fig. 4.2 compares the 8×4 pixel APDA S8550 from Hamamatsu with a PMT having typical dimensions of those used in commercial positron tomographs. In addition to the reduction in detector volume, the very small path of the charge carriers within each pixel of the APDA results in a detection efficiency, gain and timing characteristics insensitive to magnetic fields¹. This makes a silicon-based APDA a good candidate detector for the next-generation in-beam PET.

The most commonly used semiconductor detector materials are silicon and germanium, with



Figure 4.2: Photograph showing a 4×8 pixels avalanche photodiode array (left), a 1 Euro coin (middle) and a photomultiplier tube with 1 inch front window (right).

¹ Measured up to 4 T with a single-pixel APD with similar internal structure [Org02].

one electron-hole pair (e-h) produced per 3.6 and 2.8 eV of radiation energy absorbed, respectively. This is a low value compared to the ionization energy in a gas (about 30 eV) or to the approximately 300 eV necessary to extract an electron from a photocathode. Due to the small energy required to produce an e-h pair, semiconductors present a high quantum efficiency of about 70 % for light with 400 nm wavelength, which contrasts with a quantum efficiency of the order of 25 % for PMT. Gallium arsenide (GaAs), with an ionization energy of 4.1 eV, is perhaps a future alternative to silicon; presently, it seems to be an expensive and not fully mastered technology of potentially better radiation hardness [Smi96]. Similar detectors have been manufactured with diamond (13 eV/e-h) too, yielding ultra-fast, extremely radiation hard and magnetic field insensitive detectors bringing great advantages into single-particle detection or beam monitoring applications [Ber01]. Concerning photon detection with diamond, though, a quantum efficiency below 10^{-4} % has been measured with a chemical vapor deposition (CVD) detector for photon energies corresponding to wavelengths between 300 and 1200 nm [Pac00].

Semiconductor detectors have a number of problems that have limited their use in clinical practice in the past. For example, silicon and germanium conduct a significant amount of thermally induced electrical current at room temperature. Statistical oscillations in this background noise current interfere with the radiation-induced current pulses. Hence, these detectors are operated either at temperatures well below room temperature or under reverse polarization voltages high enough to produce electron multiplication within the detector, i.e. with internal gain. The principle of operation of a silicon semiconductor detector with internal amplification is shown in Fig. 4.3. The figure depicts a device optimized for the detection of short wavelength light

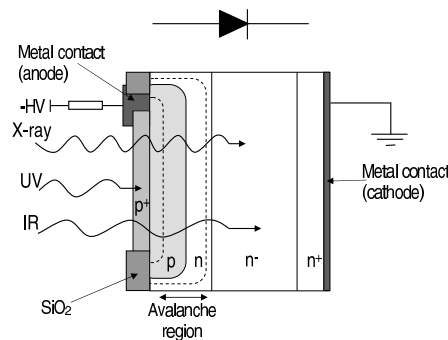


Figure 4.3: Schematic cross-section of one pixel of an APD. The high electric field at the p-n junction provides there enough energy to the drifting electrons to collide with other electrons and create more e-h pairs. This avalanche process, optimized for ultra violet photons in the figure, results in the internal gain of the APD.

(blue to ultra violet), i.e. a device where the p⁺-doped layer, laying before the amplification region composed by the p-n junction, is made small [Wil83]. This reduces the sensitivity to light in the infra-red region of the spectrum as well as to the more penetrating X-rays since these photons interact with the detector at deeper depths, generating there electrons that will not cross the amplification region during their trajectory to the cathode (the diode is reversely polarized, i.e. a positive voltage is applied at the cathode). The generated holes will drift to the anode and pass the high electric field p-n junction, but they do not achieve enough velocity to induce multiplication. Short wavelength light will interact very close to the surface and all electrons generated there have to pass the amplification region on their way to the cathode, resulting in the creation of more e-h pairs (avalanche) that will be collected in the corresponding electrodes. One immediate advantage of such an APD optimized for short wavelength detection is that the resulting nuclear counter effect is heavily minimized: the extremely small

extension of the p⁺-doped region, with typically less than 10 μm thickness [Dei00], results in a correspondingly small effective path for ionizing radiation. Minimum ionizing particles create about 100 e-h pairs per μm in silicon, but only those generated before the amplification region will be able to start an avalanche. The nuclear counter effect of an APD from Hamamatsu with very similar structure as the S8550 was measured to be as low as 5.6 μm^1 .

Radiation damage can occur via two main mechanisms: surface and bulk damage. Surface damage results from defects in the front layer of the APD, increasing the surface dark current and reducing the quantum efficiency. The total dark current I_d in an APD is given by $I_d = I_{ds} + I_{db}M$, with M the internal gain of the APD and I_{ds} and I_{db} the surface and bulk dark currents, respectively. The effect of the surface dark current plays a minor role when compared to the bulk dark current, which suffers multiplication. Bulk damage results from displacements of atoms from their lattice sites along the bulk of the APD, increasing the bulk dark current and potentially changing the APD gain for a given bias voltage. Several APD from Hamamatsu with a pixel area of $5 \times 5 \text{ mm}^2$ and with internal structure very similar to the individual pixels of the S8550 [Dei00] were irradiated with a fluence of 9×10^{12} protons per cm^2 , corresponding to 2×10^{13} neutrons per cm^2 [Huh93]. After an annealing period of 6 weeks the gain had decreased by 3%, the quantum efficiency at wavelengths smaller than 600 nm showed no remarkable differences and the dark current had increased from 2.5 to 3990 nA [Dei00]. The fluence delivered corresponds to approximately 10 years of operation of the APD at the electromagnetic calorimeter of one of the experiments (compact magnetic solenoid) of the extremely high-luminosity large hadron collider at CERN. For comparison, the mean number of carbon ions delivered at GSI to treat the first 240 patients was about 3×10^{12} . The integrated yield of light secondaries emitted in the forward semi-hemisphere, measured in [Gun04a], is about 1.7 particles per primary ^{12}C . These particles include neutrons, protons, deuterons, tritons and helium. This results in a total fluence of light particles emitted in the forward semi-hemisphere of about 5×10^{12} . For a treatment room irradiating 1000 patients per year the corresponding yearly fluence is $\leq 2 \times 10^{13}$ light secondaries emitted in the forward semi-hemisphere. Assuming the yield to be spatially homogeneous, a detector with $1 \times 1 \text{ cm}^2$ area and positioned at a distance of 1 m in the beam direction, after the target, will receive a light-particle fluence of about 3×10^8 particles cm^{-2} . This fluence is four to five orders of magnitude below that used to test the radiation hardness of the APD from Hamamatsu, described in [Huh93]. Therefore, the use of the S8550 APDA for in-beam PET is safe in what concerns its radiation hardness.

4.3 Characterization of the LSO Sample

Due to the adequate properties of both LSO as a scintillator and an APDA as a light detector for in-beam PET, a piece of LSO bought from CTI was used to prepare 64 finger-like crystals, each with $2.1 \times 2.1 \times 15 \text{ mm}^3$, in order to couple them to two APDA with 8×4 pixels each. Before fixing the crystals to the APDA their scintillating properties were investigated, namely their light yield and energy resolution, with the results shown in the present section.

4.3.1 Setup

Fig. 4.4 shows the electronics setup implemented to measure the scintillating properties of a sub-set of all 64 crystals, with the sub-set uniformly sampled in respect to the position of the crystals in the original bole. The light yield of the crystals was measured both in the vertical as well as in the horizontal position, i.e. with the $2.1 \times 2.1 \text{ mm}^2$ and the $2.1 \times 15 \text{ mm}^2$ crystal faces coupled to the window of a XP2020Q calibrated PMT from Philips Photonics,

¹ These APD were optimized by Hamamatsu in order to be used at the electromagnetic calorimeter of the future compact magnetic solenoid detector under construction at CERN [Dei00].

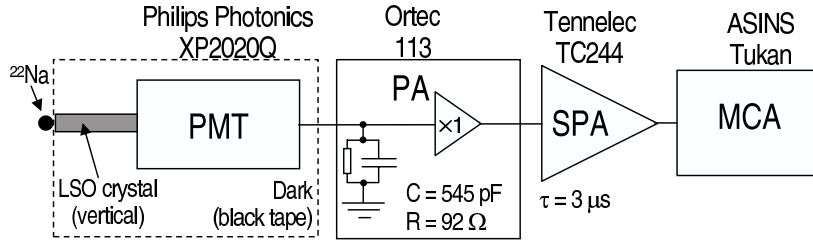


Figure 4.4: Electronics setup for characterizing the scintillation of the LSO crystals. PMT, PA, SPA and MCA denote a photomultiplier tube, a preamplifier, a spectroscopic amplifier and a multichannel analyzer, respectively.

respectively. Silicon oil was used as a coupling medium and the crystals were wrapped in several layers of teflon tape, except for the face touching the PMT. Crystal wrapping was done in a dark room in order not to induce afterglow in the scintillator. The PMT was operated at -1700 V and the signal from its anode was fed into a preamplifier (PA) model 113, from Ortec, connected with an input capacitor of 545 pF. A spectroscopic amplifier (SPA) TC244, from Tennelec, multiplied the PA signal by 1000 during the single photoelectron measurements and by 7.5 during the measurements with a ^{22}Na source. The shaping constant of the SPA was $3\ \mu\text{s}$ during all measurements. Finally, the SPA signal was fed into the multichannel analyzer Tukan, from the Andrzej Soltan Institute of Nuclear Studies (ASINS) in Swierk, Poland.

4.3.2 Light yield and energy resolution

The peak position of the 511 keV γ -quanta from a ^{22}Na source (ch_{511}) was compared to the peak position of the single photoelectron spectrum (ch_{spe}) of the calibrated XP2020Q PMT

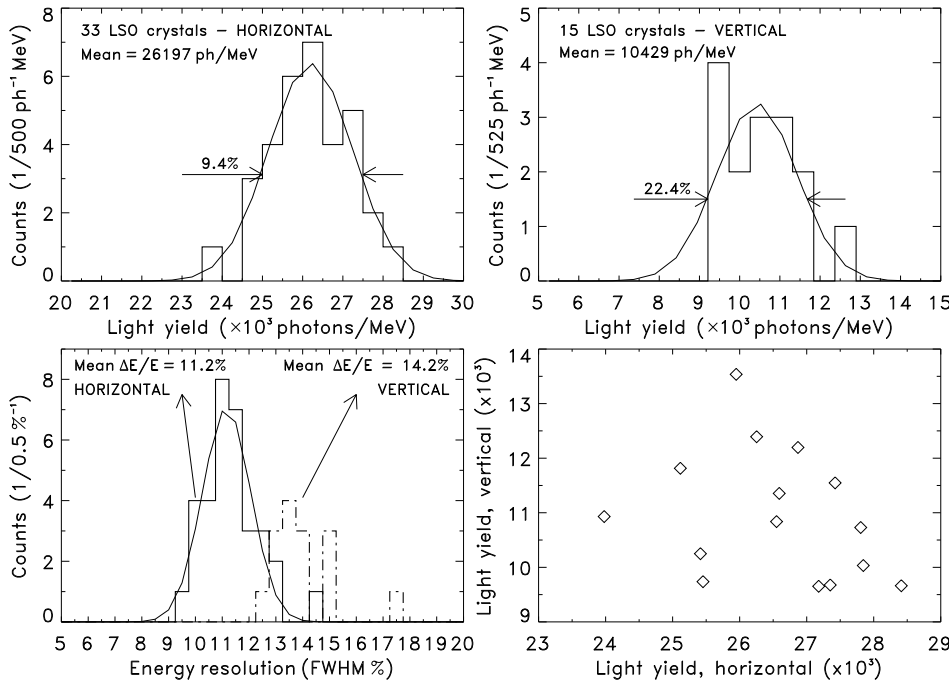


Figure 4.5: Light yield $L.Y.$ and energy resolution of the LSO samples. The top row shows two histograms with the $L.Y.$ of crystals measured in the horizontal and vertical positions (Fig. 4.4). The bottom left image shows the histograms with the energy resolutions obtained and the bottom right plot shows that there is no correlation between the $L.Y.$ measured in the horizontal and vertical positions, which means the observed $L.Y.$ dispersion is due to experimental error only.

from Philips Photonics. The light yield $L.Y.$ of each crystal, measured in photons per MeV, is calculated following

$$L.Y. = \frac{1}{\eta_{int}} \cdot \frac{1}{0.511} \cdot \frac{M_{spe}}{M_{511}} \cdot \frac{ch_{511}}{ch_{spe}}, \quad (4.1)$$

with η_{int} being the integral quantum efficiency of the PMT with respect to the emission spectrum of LSO, with a value of 20 % [Kap00], $M_{spe} = 1000$ the gain of the spectroscopic amplifier when measuring the single photoelectron spectrum and $M_{511} = 7.5$ the gain of the amplifier when measuring the spectrum with the ^{22}Na source. Fig. 4.5 shows the results obtained with the crystals in the horizontal and vertical positions, i.e. parallel to the PMT window and perpendicular to it (Fig. 4.4), respectively. The lower light yield measured with the crystals in the vertical position was expected and is due to the longer path of the scintillation photons in the crystal before reaching the PMT window. A longer path results in a higher number of re-absorbed scintillation photons due to the incomplete transparency of LSO to its own produced light. The higher number of reflections necessary in the vertical position also plays a role in justifying the lower light yield. As a consequence of a lower light yield, the mean energy resolution measured with the crystals in the vertical position (14.2 %) also deteriorates in respect to the horizontal position (11.2 %). In order to investigate whether the light yield non-uniformity of 22.4 % FWHM in the vertical position, and 9.4 % FWHM in the horizontal, arises due to experimental deviations or from a bias in the original LSO bole, the light yields in the horizontal and vertical positions are plotted against each other in Fig. 4.5. No correlation is observed, meaning that the light yield dispersion must arise from experimental error and, more importantly, all LSO crystals present similar scintillation characteristics and could, therefore, be used for the construction of the two LSO/APDA detectors.

4.4 Characterization of the APD-Array

Before coupling the LSO crystals onto the pixels of the two APDA, the properties of the APDA were studied and optimized, namely the dependence and stability of its gain with the applied reverse voltage, the shaping at the amplifier that minimizes noise readout, the ratio of light to X-ray amplification at different internal gains, the number of primary e-h pairs generated with the light from the given crystals, the energy and time resolution achievable with a ^{22}Na source, and the crosstalk between adjacent pixels with electronic and light-sharing origins.

4.4.1 Setup for DC and pulse-mode readout

The S8550 was operated in a closed, grounded metal box and the readout electronics depicted in Fig. 4.6 was implemented. Inverse polarization of the diodes was achieved with the anode

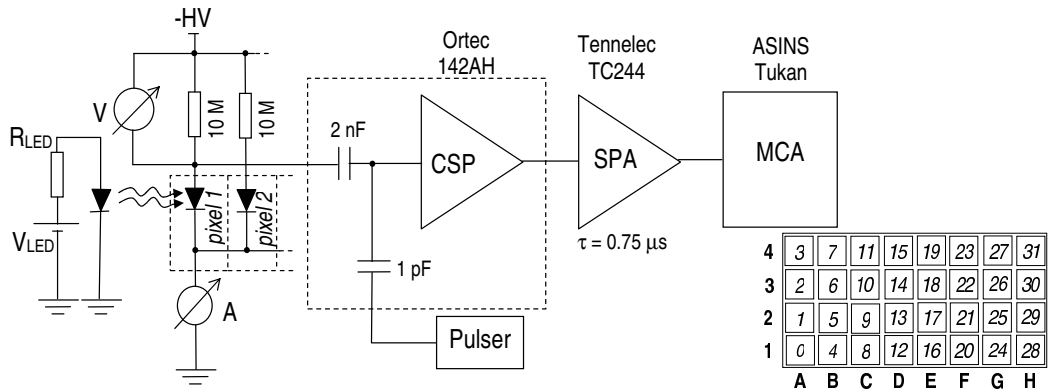


Figure 4.6: Electronics setup used for the characterization of the S8550 APDA in current and pulse modes. CSP, SPA and MCA denote a charge sensitive preamplifier, a spectroscopic amplifier and a multichannel analyzer, respectively. A front view of the APDA is shown at the bottom-right, together with the two pixel numbering schemes used: from A1 to H4 or from 0 to 31.

of each pixel connected through a resistor to the high voltage, and all cathodes connected to common ground. For the DC-gain characterization a blue LED illuminated the APD, with the current from the individual anodes read with a voltmeter at the extremes of the polarizing resistor. The current at the common cathode was read with an ampere-meter of negligible internal resistance. For pulsed light, X-ray and scintillation detection, the voltmeter and ampere-meter were substituted by the electronics depicted to the right of the 2 nF capacitor in Fig. 4.6, namely, a charge sensitive preamplifier 142AH from Ortec, compatible with detector capacities from 0 to 100 pF [Ort05], a high precision pulser PB-5 from Berkeley Nucleonics Corp. (BNC), a spectroscopic amplifier TC244 from Tenelec and a Tukan MCA from ASINS.

4.4.2 Gain characterization

For each pixel, the dark current dependence on the applied high voltage was measured with a 10 M Ω voltmeter that read the voltage drop at the polarizing resistor. The gain curve was measured similarly, with a blue light emitting diode (LED) illuminating the APDA surface in DC mode and the signal current I_{signal} calculated according to

$$I_{\text{signal}} = I_{\text{total}} - I_{\text{dark}}, \quad (4.2)$$

with I_{total} being the total current measured with the LED turned on, and I_{dark} the current measured with the LED turned off. Two types of illumination conditions were studied: single-pixel illumination and homogeneous illumination of all pixels.

Single-pixel illumination

In order to guarantee the illumination of one single pixel only, a 0.5×0.5 mm² hole was made in a black tape stripe that covered the whole APDA. The hole was matched to the center of one pixel, with active area 1.6×1.6 mm². A scan was performed with the applied high voltage and both I_{total} and I_{dark} were measured. The results from this scan are plotted in Fig. 4.7. Two regimes are clearly observed. In regime I, the e-h cloud produced by the penetrating photons is not totally collected in the corresponding cathode or anode, respectively. This is

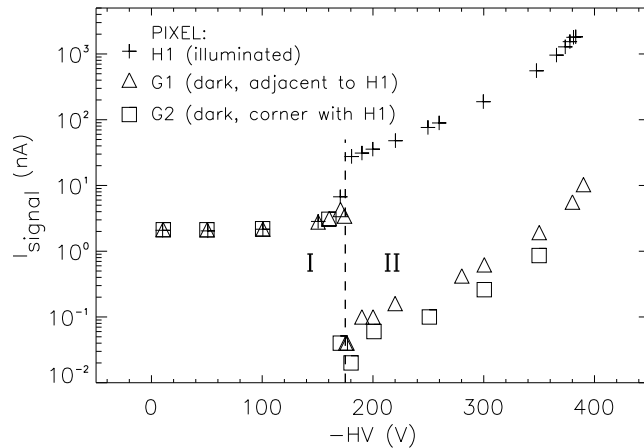


Figure 4.7: Dependence of I_{signal} on the applied voltage. In region I, before the pinch-off voltage is reached (vertical dashed line), dispersion of the e-h clouds takes place with consequent signal spread into adjacent, dark pixels. When the applied voltage is high enough to force the electric field lines to converge into the corresponding electrode only, region II is reached. There, the e-h clouds are forced to drift to the collecting electrodes and the crosstalk current drops abruptly to values below 1%. The multiplication regime takes place at higher voltages.

because the electric field lines produced by the low applied voltage are strong enough to avoid e-h recombination and start the drift, but are insufficiently strong to hold each cloud together. Repulsion disperses the formed clouds, and the hole (h) cloud which should be collected at one single pixel (anode) will spread to adjacent dark channels. A sharp step in the signal of the illuminated pixel is observed at a polarization voltage of about 173 V, which corresponds to the transition to a second regime where the pixels are individualized. The physical phenomenon behind this fact is the convergence of the electric field lines to each pixel readout region, i.e. the applied voltage has reached a value strong enough to hold the hole cloud drifting together without losses. This interpretation is confirmed by the sharp decrease of the current of adjacent dark channels (electronic crosstalk) at exactly the same voltage (Fig. 4.7). As expected, this transition voltage is not a fixed number, even for a certain pixel, and it was observed to vary slightly with the illumination conditions (next paragraph).

Homogeneous APDA illumination

With the aim of finding a reference point to normalize the output current signal and, therefore, obtain the gain evolution with the applied voltage, the current output of one pixel having the LED homogeneously illuminating the APDA surface was measured, with the result plotted in Fig. 4.8. The two different regimes described in the previous paragraph can be observed, now

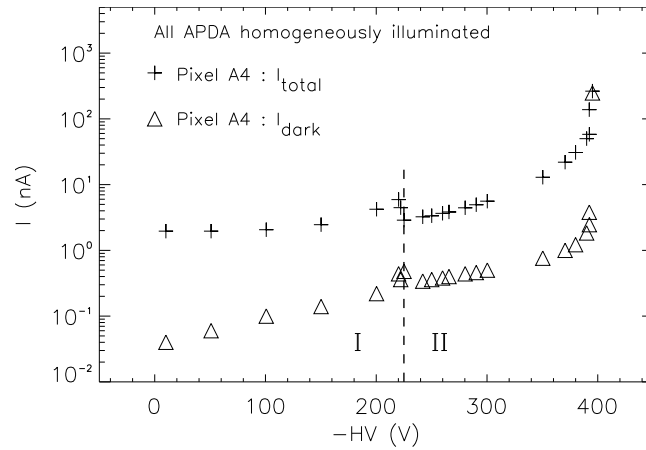


Figure 4.8: Dependence of I_{total} and I_{dark} , from a single pixel, on the applied voltage. All the APDA was homogeneously exposed to light in DC mode. Regimes I and II as in Fig. 4.7.

characterized by a sharp fall of both the total current and the dark current. This phenomenon can again be explained based on a *pixel decoupling* dependence on the applied voltage. Below the pinch-off voltage, about 210 V in this pixel, a continuous e-h cloud is created along the whole surface of the APDA, even between pixels, and the holes are being collected in the corresponding anodes. After pixelization at 210 V, the contribution from the dead areas between pixels ceases since the electric field lines, now fully connecting the anode to the cathode, do not allow signal collection from these regions. The fact that the dark current also feels this transition further confirms the described interpretation.

Gain normalization

As shown in Figs. 4.7 and 4.8, the evolution of the signal amplitude with the applied voltage strongly depends on the illumination conditions if the signal is read from the individual anodes. In order to find a reference point with unitary gain in DC mode illumination, the current signal from all diodes was read. An amperemeter with negligible internal resistance measured

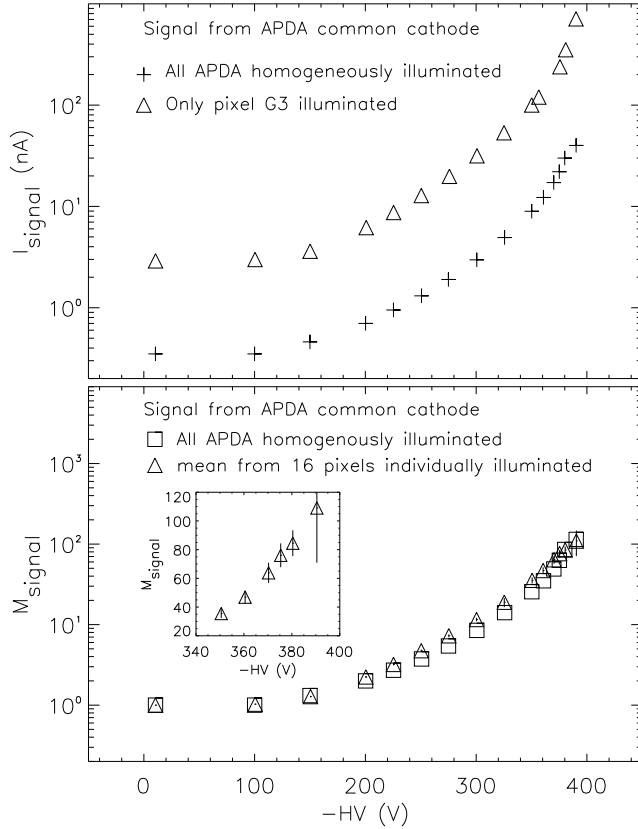


Figure 4.9: Common cathode measurements for gain normalization. The evolution of the current signal is independent on the illuminating condition (top). The different offsets (top) are due to different light intensities. The current signal yields a stable reference point for normalization of the gain (bottom). Error bars depict $\pm \sigma$ at each measured gain for the curve with the mean from 16 single-pixel measurements.

the current flowing between the common cathode of the APDA and ground (Fig. 4.6), thus eliminating the contribution from electronic crosstalk since the current contribution from all pixels is read at the same time. The top image in Fig. 4.9 depicts the obtained results. No regime change is observed, neither with single-pixel nor with full APDA illumination, since at any applied voltage all the cloud (in this case the electron cloud) is read, either from several pixels (before pixelization) or from one individualized pixel (after pixelization). Therefore, the initial flat plateau of both curves can be safely taken as a reference point with unity gain, yielding the gain curves depicted in the bottom image of Fig. 4.9. A measurement of the gain characteristics of several individual pixels resulted in a gain distribution about the mean value with $\sigma = 5$ at $M = 50$, or a σ of about 10 at $M = 80$, as highlighted in the inset.

Gain non-uniformity

In order to check the gain non-uniformity of the APDA from pixel to pixel, several spectra were acquired with a ^{55}Fe source and with the same reverse voltage. Fig. 4.10 shows results for two pixels. The standard deviation of the gain non-uniformity was found to be 4.3 % with the APDA operating at an internal gain of 61 (reverse voltage of -370.4 V).

Effective applied voltage

A 10 M Ω load resistor (Fig. 4.6) was applied to each pixel in order to keep the dark current low and, thus, increase the signal-to-noise ratio (SNR). Yet, a high load at the polarizing resistor may induce a voltage drop which can be significant if high dark currents take place or even

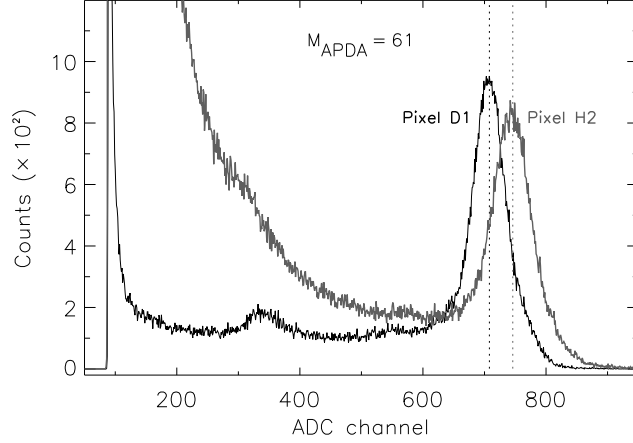


Figure 4.10: Gain non-uniformity measured between two pixels with an ^{55}Fe source. A different noise behaviour was also observed.

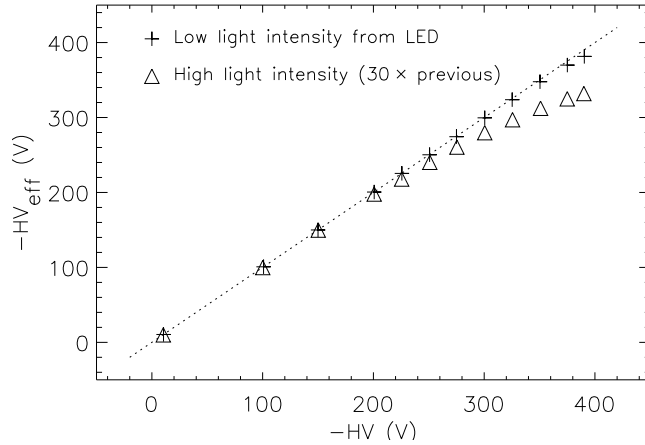


Figure 4.11: Effective voltage HV_{eff} at the APDA due to the polarizing resistor ($10\text{ M}\Omega$), with $HV_{eff} = HV - V$ (Fig. 4.6). The light intensity was adjusted by changing V_{LED} in Fig. 4.6.

if high signal currents are being measured. Such voltage drop at the polarizing resistor would result in a lower effective polarizing voltage at the diodes inducing, consequently, lower gain. Fig 4.11 confirms that the effective applied voltage does not decrease significantly for the range of voltages and dark currents studied. It also shows how a too high photon luminosity would reduce the effective applied voltage at the APDA, with a consequent non-quantified decrease in gain. For the measurement of scintillation light pulses, described in the next section, the conditions are met for stable operation since the LED provided much higher luminosity than the very weak scintillation or X-ray pulses.

4.4.3 Scintillation and X-ray detection

The APDA gain characterization presented in the previous section is also valid in pulse mode readout and is the basis for the gain knowledge of the device. In the present section the remaining performance characteristics of the APDA for scintillation detection are presented. Whenever LED light is mentioned in this section it refers to pulsed blue light, i.e. the fixed voltage supply feeding the LED in DC mode in Fig. 4.6 (V_{LED}) was substituted with a precision pulser PB-5 from BNC, yielding pulses of light instead. Whenever pulser is mentioned it refers to the known amount of charge injected directly into the electronics readout ($Q_{inj} = U_{pulser} \cdot C_{test}$) through the 1 pF test capacitor of the preamplifier (Fig. 4.6).

Noise optimization

Figs. 4.12 and 4.13 show the results obtained by scanning the amplifier shaping time τ_{AMP} at a constant reverse voltage applied, and by scanning the applied reverse voltage with a constant amplifier shaping time, respectively. Noise is quantified in units of photon energy (FWHM, eV) as well as by the equivalent noise charge¹ (ENC) at the detector level (electrons, root mean square). The difference between the normalization to the X-ray gain or to the light gain is explained in the next paragraph. Measurements above an internal gain of about 73 (Fig. 4.13) were not possible because the APDA reached breakdown, with the dark current rising steeply.

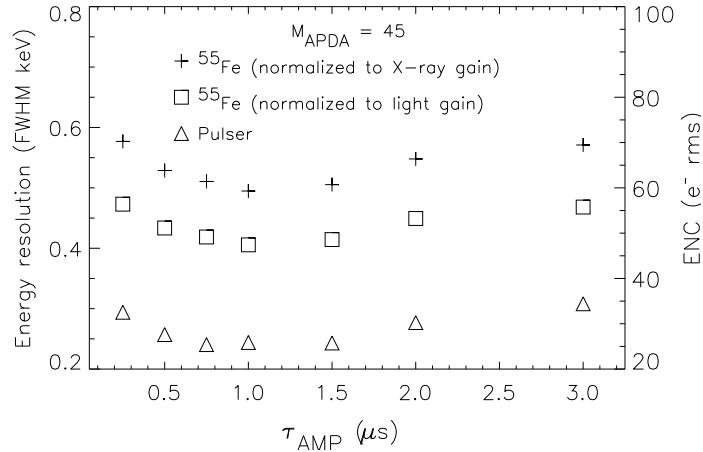


Figure 4.12: Noise dependence on the amplifier shaping time. The noise is quantified in units of photon energy (FWHM in keV, left ordinate), as well as by the equivalent noise charge (ENC) of the detector (number of electrons in root mean square, right ordinate).

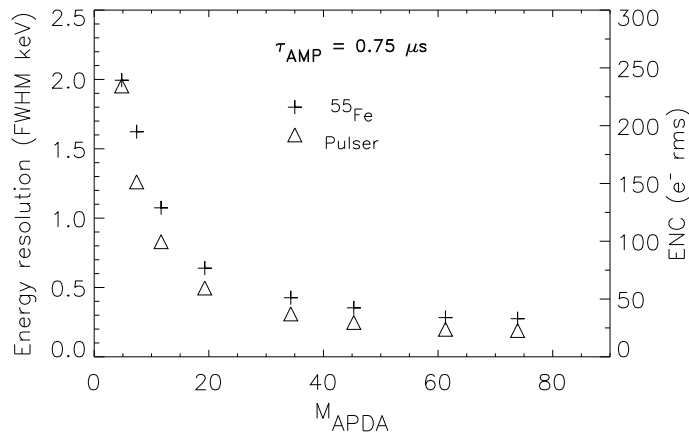


Figure 4.13: Noise dependence on the internal gain of the APDA. The noise is quantified in units of photon energy (FWHM in keV, left ordinate), as well as by the equivalent noise charge (ENC) of the detector (number of electrons in root mean square, right ordinate).

Ratio of the X-ray gain versus light gain and energy calibration

Due to its internal structure and the position of the p-n junction, optimized for the detection of light of short wavelength (Fig. 4.3), the S8550 presents different internal gains for pulsed

¹ Equivalent noise charge ENC is the quantity of charge which, appearing on the detector, would give an output pulse height with equivalent voltage measured in units of root mean square. For silicon-based detectors, $ENC = FWHM (eV) / [2.35 \times 3.6 (e-h eV^{-1})]$.

light and X-rays, with this difference increasing with the applied voltage due to the increasing extension of the avalanche region. In order to perform a precise energy calibration, the 59.5 keV X-ray peak of a ^{241}Am source was sampled with a PIN photodiode¹, together with a pulse of charge injected at the preamplifier test capacitor (Fig. 4.6). This allowed to calculate the equivalent energy delivered by the pulser [Mos01]. The gain curve obtained in the previous section (DC mode, Fig. 4.9, bottom) was then used to recalculate the pulser equivalent energies at all applied reverse voltages according to

$$E_{pulsers, M} = \frac{peak_{pulsers, PIN}}{peak_{Am, PIN}} \cdot 59.5 \text{ keV} \cdot M_{pulsers} \cdot \frac{G_{APDA}}{G_{PIN}} \cdot \frac{1}{M_{APDA}}, \quad (4.3)$$

with $E_{pulsers, M}$ the pulser equivalent energy at a device internal gain M_{APDA} . The terms $peak_{pulsers, PIN}$ and $peak_{Am, PIN}$ denote the peak positions of the pulser and the X-ray line from the ^{241}Am source measured with the PIN diode, respectively. The term $M_{pulsers}$ denotes the amplitude increased at the pulser when measuring with higher reverse voltages, and G_{APDA} and G_{PIN} are the gains set at the amplifier when measuring with the APDA and with the PIN diode, respectively. Fig. 4.14 shows the spectrum obtained with a ^{55}Fe source with the APDA operated at an internal gain of 45. The energy calibration used the method just described.

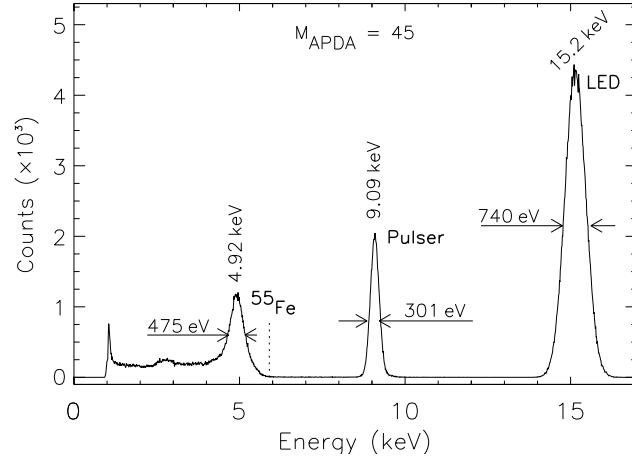


Figure 4.14: Spectrum acquired from a single APDA pixel exposed to a ^{55}Fe source, the light from a pulsed LED and a test pulser. The different APDA gain for X-ray and visible light is responsible for the shift to lower energy of the 5.9 keV X-ray peak.

Similar spectra acquired at different APDA internal gains show the light-to-pulsers ratio constant, whereas the X-ray peaks shift increasingly to smaller amplitudes. This behaviour is summarized in Fig. 4.15 for different APDA gains. It has its origin on the deeper penetration depth of X-rays into the diode, creating e-h clouds already inside the avalanche region (Fig. 4.3). These electrons create a smaller signal in respect to those raised before the avalanche region as a consequence of their shorter path through the multiplication region.

A simpler and faster calibration method, but less precise due to the intrinsic inaccuracy of the value of the test capacitor of the preamplifier, makes direct use of the amount of charge Q_{inj} injected at the test capacitor: $Q_{inj} = U_{pulsers} \cdot C_{test}$, with $U_{pulsers}$ the amplitude of the signal delivered by the pulser² and C_{test} the preamplifier test capacitor. In order to convert the injected charge into units of energy, the mean energy necessary to create an e-h pair in

¹ Photodiode fabricated with a longer, low-doped, high-resistivity intrinsic (I) region between the p-doped (P) and the n-doped (N) regions. The extended intrinsic region yields $M_{PIN}(\text{light}) = M_{PIN}(\text{X-ray}) = 1$.

² This signal must have a fast rise time t_r and long fall time t_f , approaching a step function from the point of view of the test capacitor. Typically $t_r \leq 10 \text{ ns}$ and t_f is of the order of $100 \mu\text{s}$.

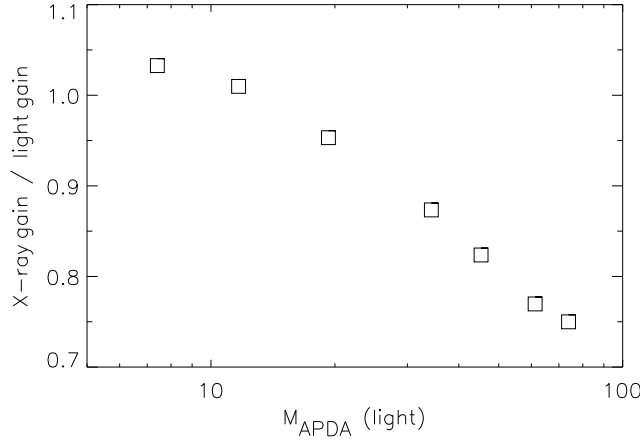


Figure 4.15: Ratio between X-ray and light gain $R_{X,light}$ for different APDA gains M_{APDA} .

silicon, 3.6 eV, is used. This method does not depend on the gain of the device:

$$E_{pulsed, M} = \frac{U_{pulsed} \cdot C_{test}}{1.6 \cdot 10^{-19} \text{ C}} \cdot 3.6 \text{ eV}. \quad (4.4)$$

Number of primary electron-hole pairs and energy resolution

The value of the ratio *X-ray-to-light-gain* ($R_{X,light}$) described above is necessary in order to calculate the number of primary e-h pairs N_{e-h} generated in the APDA at a given internal gain with a given scintillation crystal. This parameter, in turn, is important in order to compare the performance of different semiconductor-based scintillation detectors since the number of primary e-h produced per energy unit is proportional both to the energy as well as the timing resolutions achievable with the device. Fig. 4.16 shows this measurement for one pixel of the S8550 APDA. The gain of the spectroscopic amplifier in both measurements was kept at a constant value of 200, therefore a value of 4900 e-h / MeV is obtained by applying:

$$N_{e-h}/\text{MeV} = \frac{5900 \text{ eV}}{3.6 \text{ eV}} \cdot \frac{\text{peak}_{22\text{-Na}}}{\text{peak}_{55\text{-Fe}}} \cdot R_{X,light} \cdot \frac{1}{0.511 \text{ MeV}}, \quad (4.5)$$

with 5900 eV being the energy of the X-ray from the ^{55}Fe source.

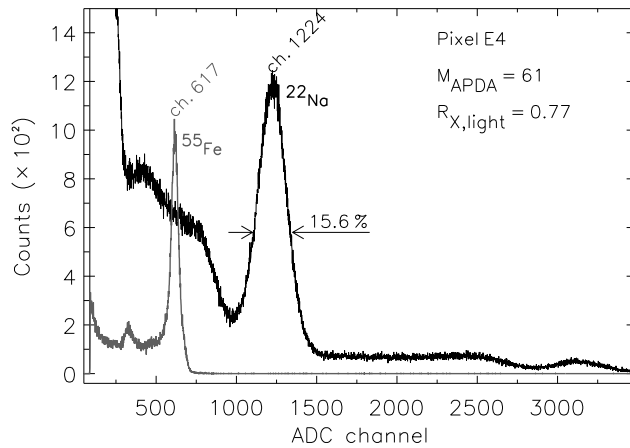


Figure 4.16: Single pixel spectra acquired with a ^{55}Fe and a ^{22}Na source, with the ^{22}Na γ -rays detected after conversion in a $2 \times 2 \times 10 \text{ mm}^3$ LSO crystal mounted in the vertical position. The reverse voltage applied to the APDA corresponds to an internal amplification $M_{APDA} = 61$, to which corresponds an X-ray-to-light-gain ratio $R_{X,light} = 0.77$.

The same value can again be calculated by injecting a known amount of charge at the test capacitor of the preamplifier:

$$N_{e-h}/\text{MeV} = \frac{U_{\text{pulser}} \cdot C_{\text{test}}}{1.6 \cdot 10^{-19} \text{ C}} \cdot \frac{\text{peak}_{22-Na}}{\text{peak}_{\text{pulser}}} \cdot \frac{1}{M_{\text{APDA}}} \cdot \frac{1}{0.511 \text{ MeV}}. \quad (4.6)$$

Although the value obtained for N_{e-h}/MeV with the S8550 is inferior to that of other devices from other manufacturers, such as the 8900 e-h/MeV measured with the same crystal with a quadrant pixel APDA from Advanced Photonix Inc. [Kap02], the device from Hamamatsu offers the advantages of being readily available even if higher quantities are requested, easy to handle due to its epoxy resin covering the front surface (windowless) and being fabricated with technology specially developed to reduce the effects of hadronic radiation.

As expected, the energy resolution measured with an APDA is worse in respect to that obtained with a PMT, even for crystals of shorter length (Fig. 4.16 versus Fig. 4.5).

Inter-pixel crosstalk

Fig. 4.17 plots the signal crosstalk measured in DC mode at different reverse voltages for one pixel (left), and measured at a device gain of 61 for a single pixel illuminated in pulse mode. The illumination conditions in both cases were described at the beginning of this section: a black tape stripe covered the whole APDA front surface except for the illuminated pixel, which was exposed to light through a hole in the tape with $0.5 \times 0.5 \text{ mm}^2$ adjusted to its center. While the crosstalk between adjacent pixels is seen to be below 1% in DC mode at all voltages above pinch-off (Fig. 4.17, left), the same value increases to about 5.7% when pulses of light

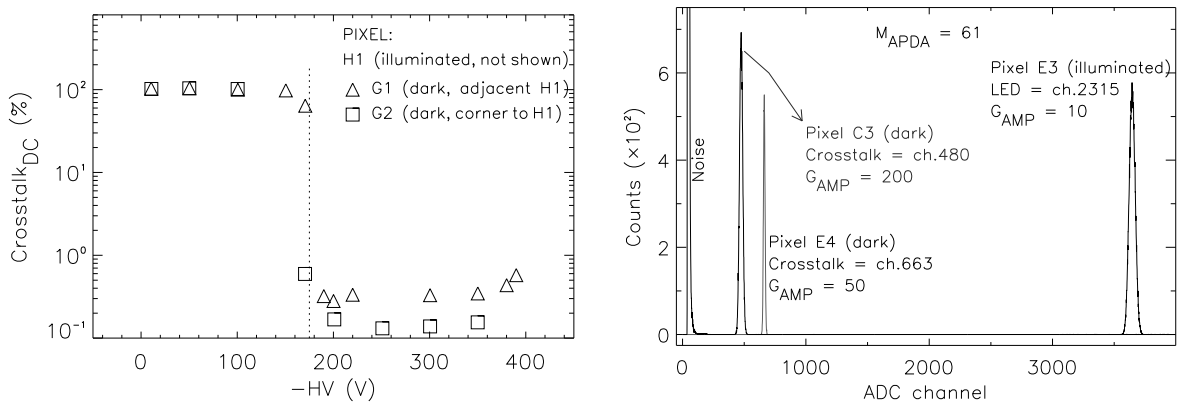


Figure 4.17: Electronic and light crosstalk in DC (left) and pulse (right) modes, measured by illuminating one pixel and reading the signal in the neighboring, dark ones.

4				5.3	5.7	0.3		
3			1.0	3.4	5.7	1.8	0.3	
2				0	0.2	0		
1								
	A	B	C	D	E	F	G	H

Figure 4.18: Crosstalk values, in percent, with pixel E3 illuminated in pulse mode. The difference observed between pixels E2 and E4 lies on the two different APDA grounds, one connecting the two upper (3 and 4) and the other the two lower (1 and 2) rows of pixels.

are detected by the illuminated pixel at a device gain of 61 (Fig. 4.17, right, pixel E3 versus E4). An inter-pixel crosstalk of about 1% is observed in Fig. 4.17, right, for non-adjacent pixels separated by one intermediate pixel (pixel E3 versus C3). Fig. 4.18 summarizes the crosstalk measurements with pixel E3 illuminated in pulse mode.

The asymmetry between the crosstalk values in DC and pulse mode was observed for other pixels as well and proves that the crosstalk measured in pulse mode is not due to light-sharing, since the illumination geometry was the same in both modes, but due to electronic crosstalk arising from the diode junction capacity and its ability to pick up a signal from current pulses propagating in its vicinity. Transient signal crosstalk induction was studied theoretically and observed experimentally in [Cre98] for charge carriers drifting in liquid xenon under an electric field, for example.

4.5 The Two LSO/APD-Array Detectors

The properties of the scintillator samples and the scintillation detector studied individually in sections 4.3 and 4.4 indicate that a low-noise signal readout electronics is required per pixel. In this section the steps taken in order to assemble the LSO/APDA detectors with minimum signal loss, both at the light collecting level due to loss of scintillation photons as well as at the signal processing due to the introduction of electronics noise, are presented.

4.5.1 Detector assembly

In Fig. 4.19 the assembly of the LSO single crystals onto the pixels of the S8550 is shown. Each pixel had all faces but one wrapped in teflon tape with 75 μm thickness, with the non-covered face fixed with silicon glue to each pixel of the APDA. The photographs in Fig. 4.19 show the crystals before covering their top surface with teflon tape.

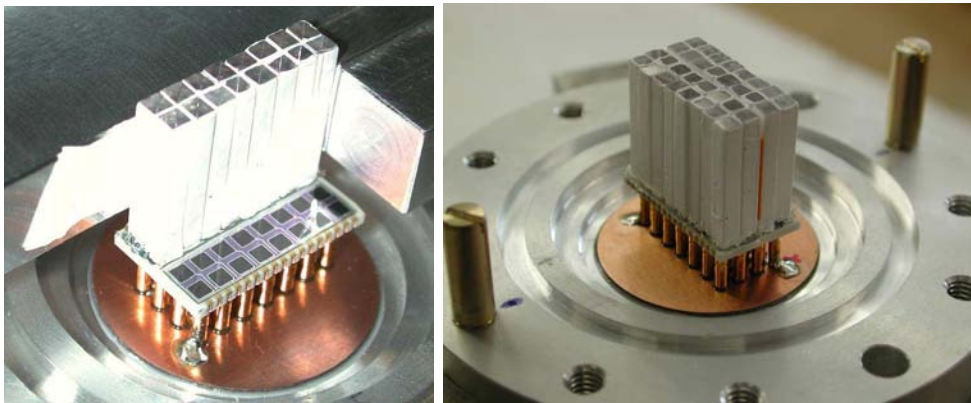


Figure 4.19: Assembly of the LSO single crystals onto the pixels of the S8550. The APDA pins are connected to a circular copper disk, seen below the device, with a diameter of 26 mm.

Silicon glue was used to fix the LSO crystals to the APDA after a seven days test that compared the light collected with glue and with high viscosity silicon oils up to a viscosity factor of 2 million. During the first day the oil creeps along the teflon tape and makes it transparent to light, resulting in a decrease in light collection of 2.5% measured after 12 hours, together with a decrease in energy resolution of 1.9% measured with an XP2020Q PMT and with a $2.1 \times 2.1 \times 15 \text{ mm}^3$ crystal coupled to it in the vertical position. This effect does not take place if silicon glue is used since it solidifies in less than one hour. Furthermore, by using glue, crystal displacements during detector handling at a later stage are avoided.

4.5.2 Energy and timing signal splitting at the preamplifier

The LSO/APDA detectors were later covered with an aluminum box, shown in the left photograph of Fig. 4.20, that guaranteed complete darkness at the detector level. Also shown in both photographs are the ventilated aluminum boxes containing the 32 charge sensitive preamplifiers (CSP) that read each detector pixel individually. The CSP were developed at ASINS, in Swierk, Poland, for these specific detectors [Kap04]. Each CSP provides two outputs: a fast, negative-shape signal for timing applications and a slow, positive-shape signal for energy readout (Fig. 4.21). This splitting simplifies the electronics for signal processing at this study stage with two detectors only. It obviously does not provide a final solution if these detectors should be applied in a real tomograph with thousands of readout channels. The decision for signal splitting was based on the advantages of implementing an optimum, but slow, noise-

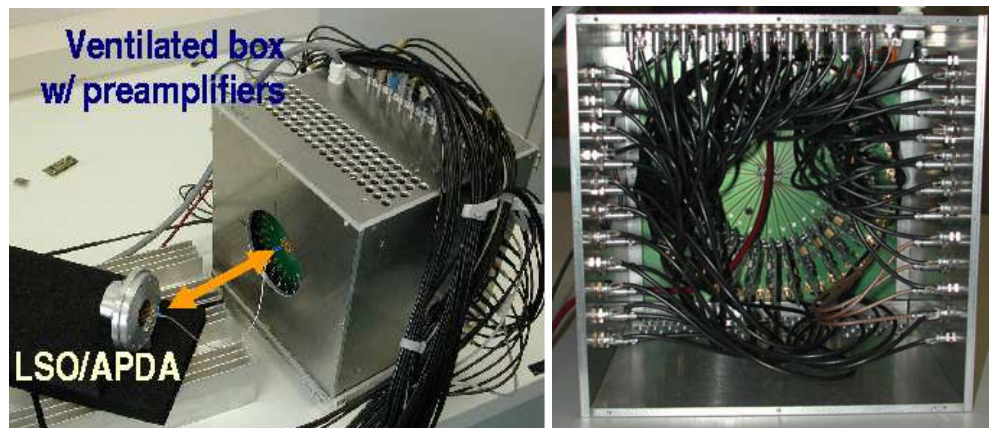


Figure 4.20: Front and back views of one detector head. The LSO/APDA detector (left) is enclosed in a light-proof, aluminum box. The detector connects to a motherboard containing 32 charge sensitive preamplifiers (CSP) through its back pins (arrow). The right photograph shows the back of the CSP box without the cover and the ventilator.

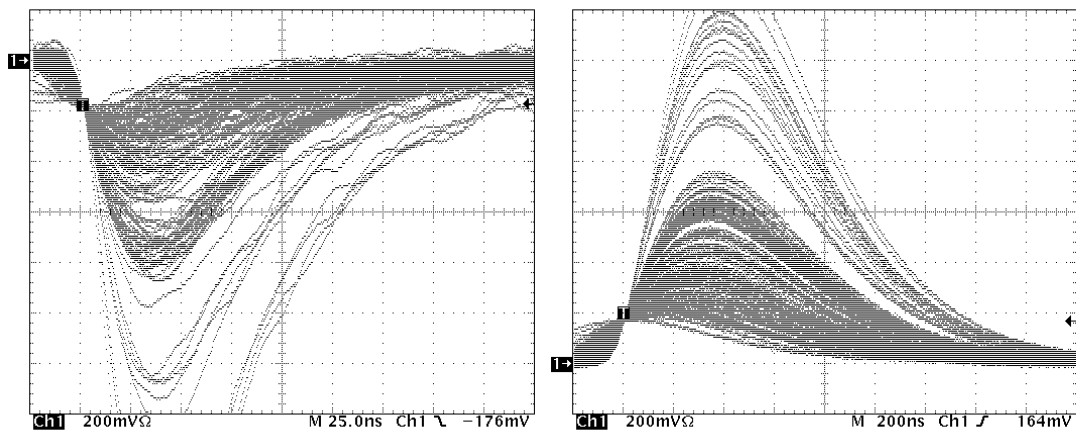


Figure 4.21: Fast (left) and slow (right) outputs from one pixel with a ^{22}Na source irradiating the whole detector. Several signals are superimposed, allowing the lines corresponding to the interaction of a 511 keV photon to be seen. The fast output was sampled after the preamplifier and a DC amplifier with gain 10. The slow output was sampled after the preamplifier and an amplifier with $0.5 \mu\text{s}$ shaping constant and gain ≥ 10 . Both signals were read with a 50Ω input resistance at the scope.

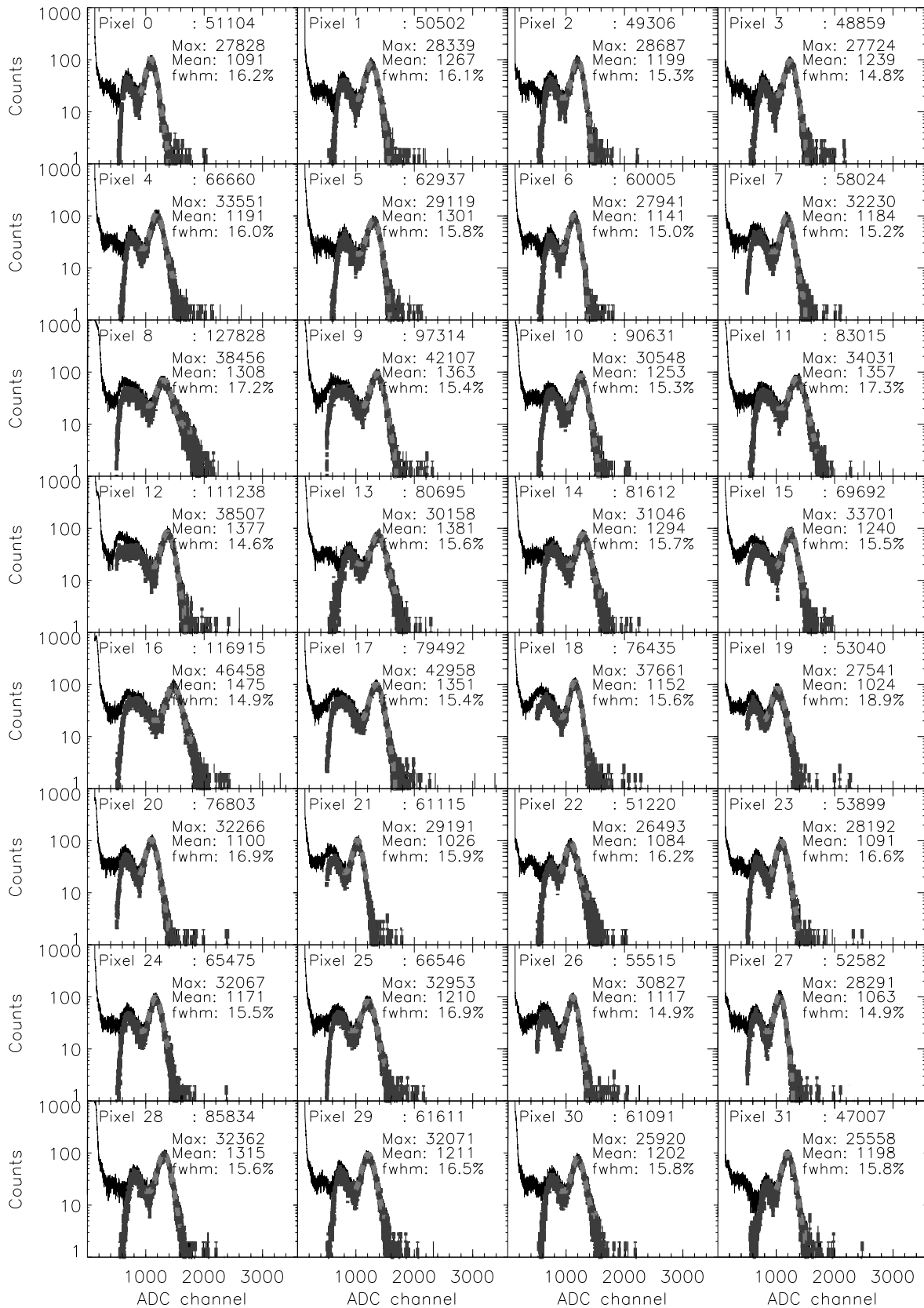


Figure 4.22: Energy calibration of detector 1 with a ^{68}Ge line source. Shown for each pixel: total counts above channel 128 (i.e. above noise), number of counts where a maximum energy deposition took place in that pixel, mean of the fit to the 511 keV full-energy peak and the corresponding FWHM. A low energy threshold was set between ADC channels 500 and 600, corresponding to about 250 keV. The gray line plots the spectrum with maximum events only.

reduction shaping constant at the energy signal, seen in section 4.4, together with a fast, but noisier, timing output optimized for the fast decay time of LSO.

4.6 Imaging Properties of the LSO/APD-Array Detectors

In this section the detector properties influencing the imaging performance of the two detectors are described. These are important parameters later used for image quantification in the following chapters 5 and 6. The electronics chain implemented to operate the two detectors in coincidence is detailed in section 5.2. In section 6.3 this electronics chain is further enhanced in order to allow the suppression of random events during in-beam PET measurements. Finally, appendix B describes the data acquisition system implemented for event readout. The results presented in this section concern measurements made with radioactive sources only.

4.6.1 Energy and time resolution

The mean energy resolution obtained both with a ^{68}Ge line source and a ^{22}Na point source for the 64 channels is $15.5 \pm 0.4\%$ FWHM. Fig. 4.22 shows the energy spectra of one detector obtained with a line source of ^{68}Ge scanned in the mid-plane between the detectors, with these operated in coincidence. The measured coincidence time resolution is 6.2 ± 0.2 ns FWHM, slightly worse than the 3.0 ± 0.2 ns FWHM extrapolated from a measurement against BaF_2 and obtained for one single pixel in [Kap03]. The slightly worse time performance was expected and arises from two factors: the longer LSO crystals used, 15 mm versus 10 mm in [Kap03], respectively, and, more importantly, the increased number of channels in these measurements which introduce a higher time spread at the electronics level.

4.6.2 Scanned line source measurements and image fill factor

For image reconstruction as well as to check the stability of the detectors the individual detection efficiency of the lines-of-response (LOR) between all detector crystals has to be known. In order to measure this, a ^{68}Ge line source has been moved centrally between the detectors in steps of 0.5 mm. Fig. 4.23 shows the results from two measurements performed at stabilized temperature, at different days and in different rooms. Stable results with identical profiles were obtained, together with similar standard deviations of the number of counts per LOR. The different mean numbers of counts per LOR obtained between the top and bottom results in Fig. 4.23 is expected due to two factors: the setups had different coincidence solid angles, with the distance between the detectors being 212 mm and 112 mm, respectively, and the acquisition times differed from 5 min/step versus 2 min/step, respectively. From this, a ratio of the mean counts per LOR can be predicted:

$$\frac{N_{212}}{N_{112}} = \frac{5 \text{ min}/(212 \text{ mm})^2}{2 \text{ min}/(112 \text{ mm})^2} = 0.698. \quad (4.7)$$

N_{212} and N_{112} denote the mean number of counts for scans with the detectors 212 mm and 112 mm apart, respectively (Fig. 4.23). The measured versus expected ratios agree to about 4% if the measured numbers of counts are properly corrected against the acquisition dead time. This is necessary since during the measurements the dead time of the acquisition system decreases as one moves the source from the centre of the field-of-view (FOV) to the edges.

The images in the left column of Fig. 4.23 contain the solid angle dependence of each voxel in the image central plane, weighted by the different efficiencies of each LOR intersecting it, i.e. they are the basis for normalization of all further images backprojected into the central plane. These images allow to quantify the intensity of any mid-plane image in absolute terms, provided that

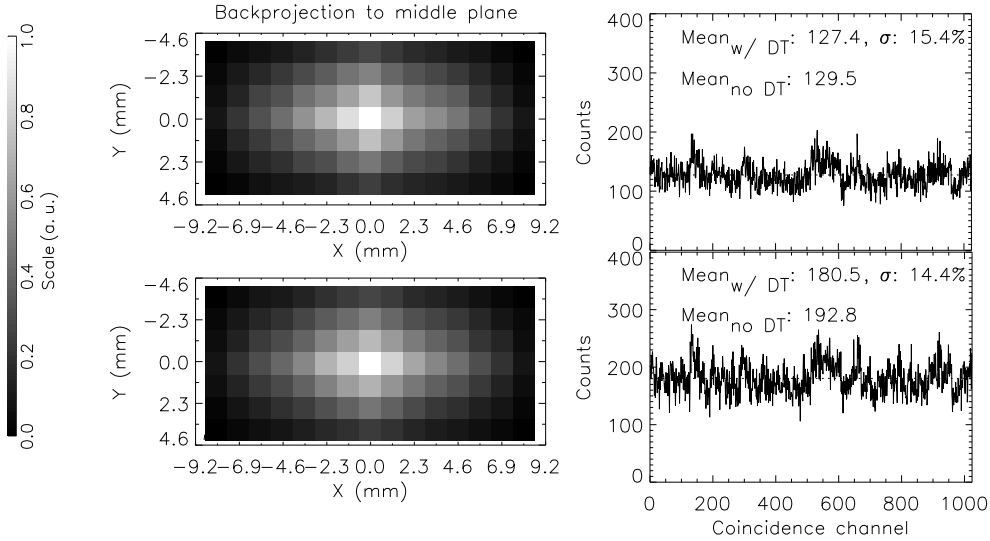


Figure 4.23: Results of the scanned line source measurements. The top row corresponds to a distance of 212 mm between the detectors, with 5 minutes acquisition/step, whereas the distance in the bottom row was 112 mm, with 2 minutes acquisition/step. Each coincidence channel (LOR) contains the number of events with energies within the photopeaks (FWHM) in both hit crystals. $Mean_{w/DT}$ and $Mean_{no DT}$ are the mean number of counts with and without dead time influence, respectively. The X and Y axes define the mid-plane between the detectors.

it was acquired with the same detector geometry and that the coincidence detection efficiency of the central voxel is known (section 4.6.3). For that, a multiplicative factor named image fill factor Π must also be known:

$$\Pi = \frac{\sum_{i,j}^{N_x, N_y} \cdot \Omega_{i,j}}{\sum_{i,j}^{N_x, N_y}}, \quad (4.8)$$

with N_x and N_y the number of image voxels in the X and Y directions, respectively, and $\Omega_{i,j}$ the solid angle of image voxel $\{i,j\}$. This image fill factor quantifies the mean difference between all image voxels shown in Fig. 4.23 and unity, with unity verified at the very central voxel (100 % relative intensity). Its value, used for image quantification in chapters 5 and 6, was calculated from Eq. 4.8 to be 30.5 % for the mid-plane images of Fig. 4.23. A similar procedure was applied to any other backprojection onto another plane between the two opposing detectors.

4.6.3 True coincidence detection efficiency

In order to estimate the true coincidence detection efficiency of two crystals forming a LOR the scanned line source measurement with detectors being 112 mm apart was considered (Fig. 4.23, bottom). Since the diameter of the ^{68}Ge rod source used is larger than the edge of the crystals, 3 mm versus 2.10 mm, respectively, a simulation was carried out in order to estimate the mean solid angle that sees the activity at the central plane as the line source is scanned, as depicted in Fig. 4.24.

Table 4.2 shows the parameters used to estimate the true coincidence detection efficiency within a LOR. The mean number of detected events per LOR, N_d , already includes the correction for the dead time of the data acquisition system. The mean solid angle, $\overline{\Omega}_9$, has been calculated from the ratio between the pairs of photons hitting the front surfaces of the opposing crystals (Fig. 4.24) and the total number of histories. The acquisition time, Δt , is weighted by 9 due

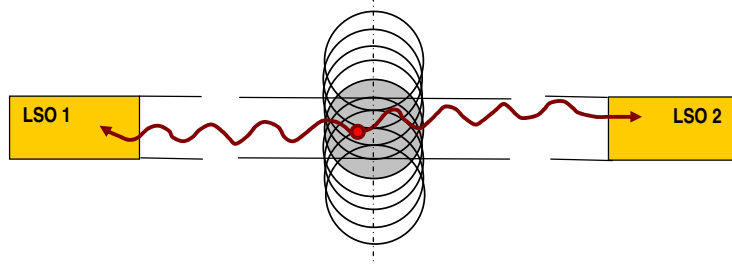


Figure 4.24: Geometry used to simulate the solid angle of a LOR between two opposing crystals. The line source, with 3 mm diameter, lies perpendicular to the image plane and is scanned with steps of 0.5 mm. For each position i of the source, ten million annihilation photon pairs were started. The ratio of photon pairs impinging on the detectors surfaces over the number of events started defines the solid angle Ω_i of each position.

Table 4.2: Parameters used for the true coincidence detection efficiency estimation.

Detected coincidences	N_d	192.8
Source activity (^{68}Ge) / 2 mm	A_{rod}	238.6 kBq
Mean solid angle (9 positions)	$\overline{\Omega}_9$	1.52×10^{-5}
Acquisition time (9 positions)	Δt	9×120 s
Expected coincidences	N_e	3917
Photons on detector surfaces	$(1 - \epsilon_{Al})^2$	88.9 %
Absorption in LSO	ϵ_{LSO}^2	53 %
Double photoelectric interaction	ϵ_{ph}^2	15 %
Within FWHM	ϵ_{fwhm}^2	57.8 %

to the fact that $\overline{\Omega}_9$ is the mean of 9 rod source steps:

$$\overline{\Omega}_9 = \frac{1}{9} \sum_0^8 \Omega_i, \quad (4.9)$$

with Ω_i defined in Fig. 4.24. The expected number of coincidences is the product

$$N_e = A_{rod} \cdot \overline{\Omega}_9 \cdot \Delta t, \quad (4.10)$$

and so the true coincidence detection efficiency ϵ_{LOR} is

$$\epsilon_{LOR} = N_d / N_e = 4.9\%. \quad (4.11)$$

On the other hand, this efficiency can be calculated according to

$$\epsilon_{LOR} = (1 - \epsilon_{Al})^2 \cdot \epsilon_{LSO}^2 \cdot \epsilon_{ph}^2 \cdot \epsilon_{fwhm}^2, \quad (4.12)$$

with $(1 - \epsilon_{Al})^2$ the fraction of photon pairs penetrating the 1.5 mm thick detector aluminium covers and reaching the surfaces of the crystals, ϵ_{LSO}^2 the part of photons absorbed in the LSO crystals, ϵ_{ph}^2 the probability that both annihilation photons interact by means of the photoelectric effect with LSO [Mos96] and ϵ_{fwhm}^2 the fraction of photon pairs falling within the FWHM in both peaks. Taking the values listed in Table 4.2 into Eq. 4.12 gives $\epsilon_{LOR} = 4.1\%$, which is in a reasonable correspondence with the value calculated with Eq. 4.11 if the rather simple model is taken into consideration.

4.6.4 Inter-pixel light crosstalk

An inter-pixel crosstalk of less than 10 % was observed between adjacent pixels. Fig. 4.25 shows the influence of the crosstalk signal from the detection of positron annihilation γ -rays in pixel A1, positioned at the corner edge of detector 1, onto the spectra of its directly adjacent pixels. It can be seen that almost all full-energy events occurring in pixel A1 generated a crosstalk signal in its edge-neighboring pixels A2 and B1. The low-energy peak observed in corner-neighbor pixel B2, with less counts and a mean energy well below 55 keV, was expected since the smaller surface contact between both pixels decreases the number of scintillation photons crossing between pixels.

The inter-pixel light crosstalk values measured do not play a major role for the detection of positron annihilation since they amount to energy values close to the noise level and, therefore, any readout threshold will discard them. This is no longer the case if higher energy events are to be read since a 5 MeV signal occurring in a given pixel, for example, will induce a 500 keV signal in its neighbors, as detailed in [Cre05d] and in section 6.9.3.

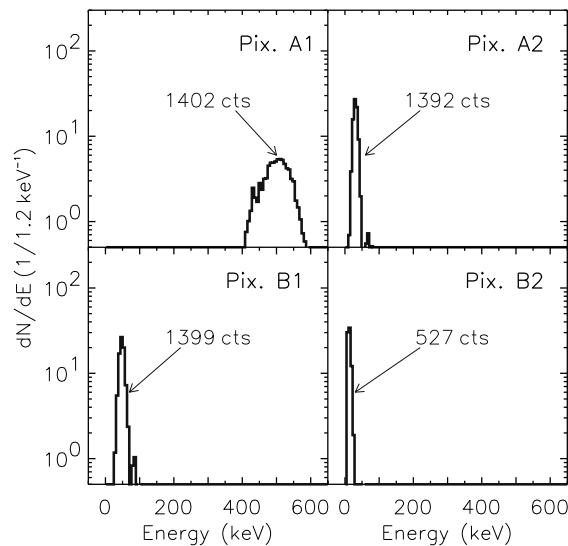


Figure 4.25: Light crosstalk within the pixels of the assembled detector. The γ -rays with 511 keV which deposit their full energy into pixel A1 leave a small crosstalk signal in their directly adjacent neighbor pixels A2 and B1. Corner-adjacent pixel B2 registers a smaller number of crosstalk signals with less amplitude, as expected due to geometrical reasons.

4.6.5 Temperature stabilization

Fig. 4.26 puts in evidence the need for a stabilized temperature. The top row shows one of the measurements of Fig. 4.23 but displayed with solid angle correction. The bottom row shows a measurement where the temperature was changed during the line source scan. The dramatic change in detector efficiency with the temperature is reflected in the strong inhomogeneity of the bottom image.

Fig. 4.27 shows the energy resolution degradation with changing temperature. As expected from the APDA gain temperature coefficient of $-2.4\% / \text{K}$ [Mos03], the photopeak shifts to the left with higher temperature, yielding non acceptable energy resolution values. The effect on the coincidence time resolution is not seen since it is smaller than the time spread introduced by the independent signal processing hardware of the 64 timing channels. Temperature stability at the detector level was achieved approximately 40 minutes after turning on all electronics,

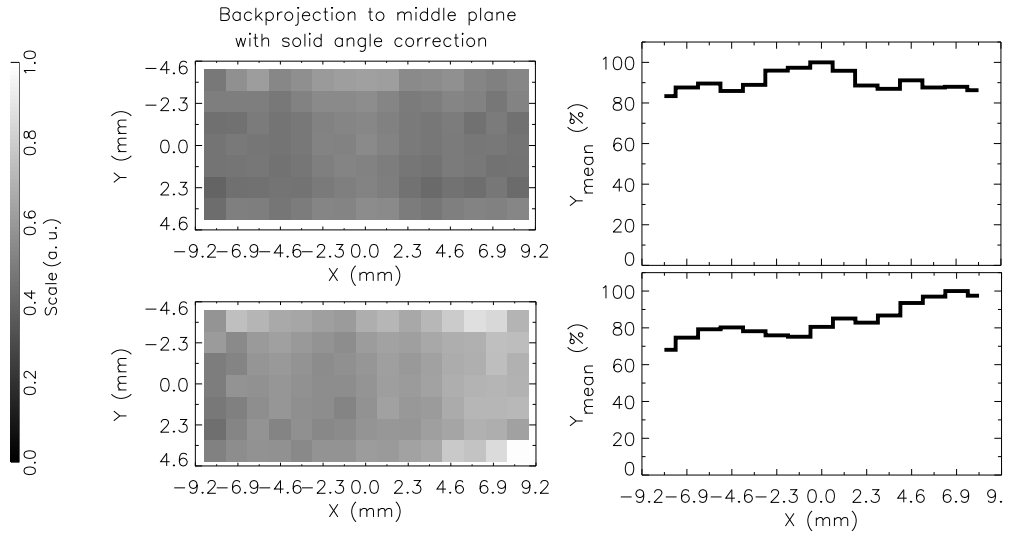


Figure 4.26: Influence of the temperature on the detector sensitivity. The plots on the left column were obtained by backprojecting the events acquired with a scanned line source onto the central plane between the detectors (112 mm distance, 2 min/step). Each image voxel is corrected for its solid angle weight. The right column shows the normalized projections of these images onto the X axis. The top measurement was performed with a stabilized temperature, whereas at the bottom a temperature change of about 5 K took place. Axes and intensity scale as in Fig. 4.23.

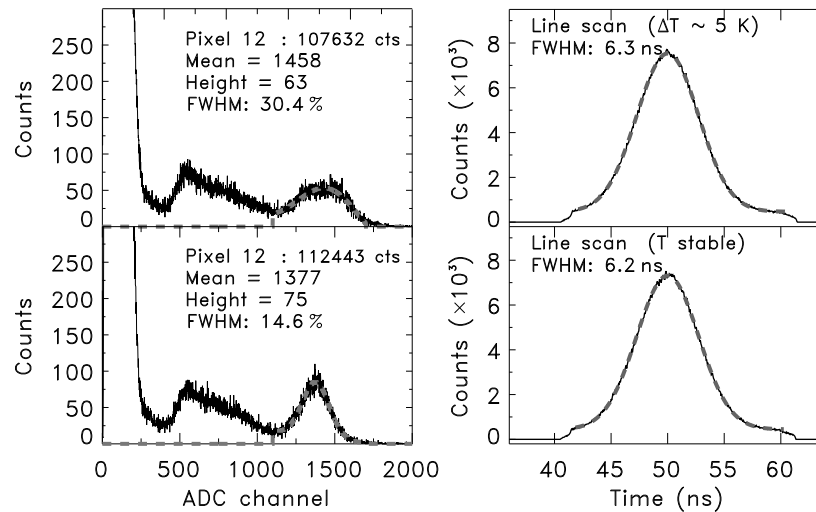


Figure 4.27: Influence of temperature drift on energy and time resolution. The top row shows the effect of a continuous temperature drift on the energy and time spectra. The bottom row shows spectra acquired with a stable temperature (measurement performed at equilibrium after the initial rise in temperature finished).

and with a normal air-conditioning room temperature control. This was verified by performing all day measurements without photopeak shifts observed. Both detector preamplifier boxes were ventilated with a small fan avoiding temperature gradients between the ambient and the detectors and preamplifiers.

4.7 Summary and Outlook

The next generation in-beam positron emission tomograph to be installed at the dedicated heavy ion facility in Heidelberg is to be operated close to the last magnet of the rotating medical beam line. Experimental results from the literature, combined with conservative calculations of the fringe magnetic field expected outside the mentioned magnet, show that the presently used photomultiplier tubes do not provide enough magnetic field resistance, even when covered with an optimum magnetic field shield such as mu-metal sheets. In addition, spatial restrictions arise due to the number of diagnostics instrumentation to be installed at the patient treatment site, which make a reduction of the in-beam PET detector volume very desirable. The substitution of PMT by state-of-the-art avalanche photodiode arrays APDA for scintillation light detection provides an answer to this two requisites. Their combination with recently commercially available, fast scintillators such as cerium-doped lutetium oxyorthosilicate LSO further enhance the performance of the next-generation in-beam PET detectors, namely better time and energy resolution can be achieved in respect to the presently installed detectors. These parameters are directly related to the quality of PET images. They are, furthermore, essential for in-beam PET readout during beam extractions in order to suppress the high yield of background events registered there, as presented in chapter 6.

Because of the advantages mentioned in the previous paragraph, two detectors each consisting of finger-like LSO crystals individually coupled to the 32 pixels of an APDA from Hamamatsu were assembled after the optimum parameters for signal maximization have been studied, namely the use of silicon glue for crystal coupling, teflon tape as a scintillation light reflector outside each crystal, high voltage value optimized for minimum signal noise and readout electronics adapted to the time and energy constraints of the detector. The measured energy and time resolutions of $15.5 \pm 0.4\%$ FWHM and 6.2 ± 0.2 ns FWHM, respectively, are below those of the BGO/PMT-based tomograph presently installed at the therapy unit at the Gesellschaft für Schwerionenforschung at Darmstadt. Nevertheless, the electronics strategy implemented, with two shaping channels implemented per pixel optimized for energy and timing reading, is by no means feasible in a clinical tomography system with thousands of channels. This dual-channel strategy was adapted here only to make possible a straight-forward study of the performance of the detectors under irradiation conditions, as presented in chapters 5 and 6.

In addition to the assembly and readout optimization of the detectors, the last section in this chapter summarizes the imaging properties of the two LSO/APDA detectors operated in coincidence. Based on several flood source measurements performed with a line source, the solid angle of the image voxels in the mid-plane between the detectors was quantified and the coincidence detection efficiency for one LOR was calculated, providing the parameters for image quantification during the in-beam imaging experiments described in chapters 5 and 6. Ambient temperature was found to be an important parameter affecting the performance of the detectors and influencing their imaging sensitivity. Therefore, measures for temperature stabilization were taken. It was experimentally verified that stable measurements can be performed when equilibrium between the ventilated detector heads and the air-conditioned experimental room is reached, which takes place approximately 40 minutes after the detector power supplies are switched on.

The studies exposed in the present chapter provided the basic detector operation knowledge for the next two chapters.

Chapter 5

Feasibility of an LSO/APDA-Based Tomograph with Small Gaps

5.1 Motivation

Due to the promising clinical results achieved at the German heavy ion tumor therapy pilot project (chapter 1), a hospital-based facility is being constructed at the university clinics of Heidelberg, Germany, and additional facilities are being planned elsewhere [Sie04]. At the Heidelberg facility, for example, delicate therapeutic situations are expected to be treated with a rotating beam delivery (gantry, chapter 3) preferentially equipped with a dedicated in-beam PET system. Fig. 5.1 depicts this system, with a gap between the two detector heads considered in order to (1) provide an entrance for the primary beam, occupying a maximum area of $20 \times 20 \text{ cm}^2$, and (2) an escape port for the flux of light fragments, mainly neutrons and protons [Gun04a, Gun04b], leaving the patient downbeam.

In chapter 2 it was shown that the detectors of such a PET system should cover a large solid angle, forming a double-head tomograph with small gaps in order to minimize image artifacts. Furthermore, the detectors should be of small volume, minimal weight and resistant to magnetic fields due to the proximity to the beam bending magnets (chapter 3). The combination of crystals of cerium-doped lutetium oxyorthosilicate ($\text{Lu}_2\text{SiO}_5:\text{Ce}^{3+}$, LSO) and avalanche photodiode arrays (APDA), described in chapter 4, could solve these problems. While similar detectors have shown their applicability to tracer imaging [Pic01], their performance for in-beam PET was unknown. Therefore, an experimental study of the proposed detectors before a final design of the next-generation in-beam PET scanners was necessary. For this reason, the performance and in-beam imaging capabilities of the two position sensitive γ -ray detectors described in chapter 4, each consisting of a Hamamatsu APDA (S8550) with its pixels individually coupled to single LSO crystals, were investigated and summarized in [Cre04] and [Kap04], with a more detailed analysis presented here.

The two detectors were operated in coincidence at the medical beam line of the Gesellschaft für Schwerionenforschung (GSI) in Darmstadt, Germany. In a first set of experiments their imaging performance was tested before, during and after the irradiation of phantoms of polymethylmethacrylate (PMMA) with a carbon ion beam with fluence equivalent to 1 000 typical daily therapeutic fractions. In these experiments the detectors were positioned both upbeam as well as downbeam from the irradiated target, forming small angles with the beam direction in order to investigate the performance of detectors laying at these critical points.

A second set of experiments, performed after the irradiation with high fluences, tested the in-beam imaging capability of these detectors in conditions that simulate the in-beam patient irradiation: The depth distribution of positron emitter radionuclides created in a phantom that stopped the high energy carbon ion beam were imaged by making use of the accelerator status information for selecting events acquired during the extraction pauses only.

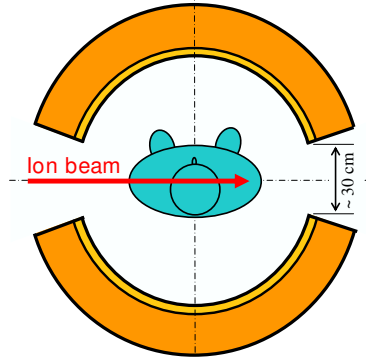


Figure 5.1: Scheme of the PET detector configuration under study for the next-generation, in-beam PET scanners.

Since previous in-beam PET research in Berkeley was abandoned due to detector activation (Bismuth Germanate, $\text{Bi}_4\text{Ge}_3\text{O}_{12}$, BGO) arising most probably from secondary particles caused by the passive beam shaping components [Lla88], the possible activation of the scintillator material LSO by the flux of light particles leaving the patient downbeam [Gun04a, Gun04b] was investigated. For that, two patients with single irradiation portals were selected and a small matrix of crystals was placed in their masks downbeam, following the beam direction with maximum penetration depth in order to meet the expected maximum light particle flux leaving the irradiated patient. High resolution spectroscopic measurements of the crystals irradiated in the described way were then performed and compared with measurements made before the irradiation.

The influence of the natural background activity density of LSO onto the random coincidences background expected for a tomograph with the geometry proposed in this chapter is also addressed. Natural lutetium contains 2.6 % of the isotope ^{176}Lu , which decays with a half-life of about 3.8×10^{10} years by β^- emission, followed by a γ -ray cascade. This results in an LSO background activity density of 240 Bq cm^{-3} [Hub02]. Calculations show that suppressing this background is essential in order not to compromise the images taken by LSO-based, in-beam PET scanners. Nevertheless, randoms subtraction techniques fail for in-beam PET measurements during particle extraction, which are mandatory for the next-generation tomographs to be operated under optimized accelerator particle delivery (chapter 6). Therefore, a modern readout scheme, capable of decreasing the coincidence time resolution obtained with conventional nuclear electronics, is proposed. Alternatively, a recently developed scintillator with reduced background but less detection efficiency in respect to LSO is also considered.

Finally, the impact of recent developments in ultra-fast timing detectors, potentially allowing the implementation of the time-of-flight (TOF) technique onto commercial PET scanners, is extrapolated to in-beam PET. It is shown that TOF techniques gain much importance for dual-head, in-beam PET scanners due to the capability of the TOF information to reduce the image elongation that characterizes limited-angle tomography. Equally important, both for closed-ring as well as for dual-head, in-beam positron tomographs, is the immense decrease in data processing time if the TOF information is used [Cre05a], making in-beam PET images available even during the irradiation for tomographs with a coincidence time resolution below 200 ps FWHM.

In summary, the studies presented in this chapter, performed under high beam fluences and, therefore, providing high count rates for the PET measurements, are conclusive in what regards the capability of performing in-beam PET imaging with detectors positioned at small angles with the beam direction.

5.2 Electronics Setup for In-Beam Imaging

In order to assess whether photon detectors consisting of LSO crystals coupled to APDA are a feasible solution for this next generation of in-beam PET, the two LSO/APDA detectors described in the previous chapter were operated in coincidence at the GSI medical beam line. Each detector consists of 32 LSO crystals ($2.1 \times 2.1 \times 15 \text{ mm}^3$ each) coupled individually to the 4×8 pixels of a Hamamatsu S8550 APDA with silicon glue (chapter 4). Fig. 5.2 shows the fast-

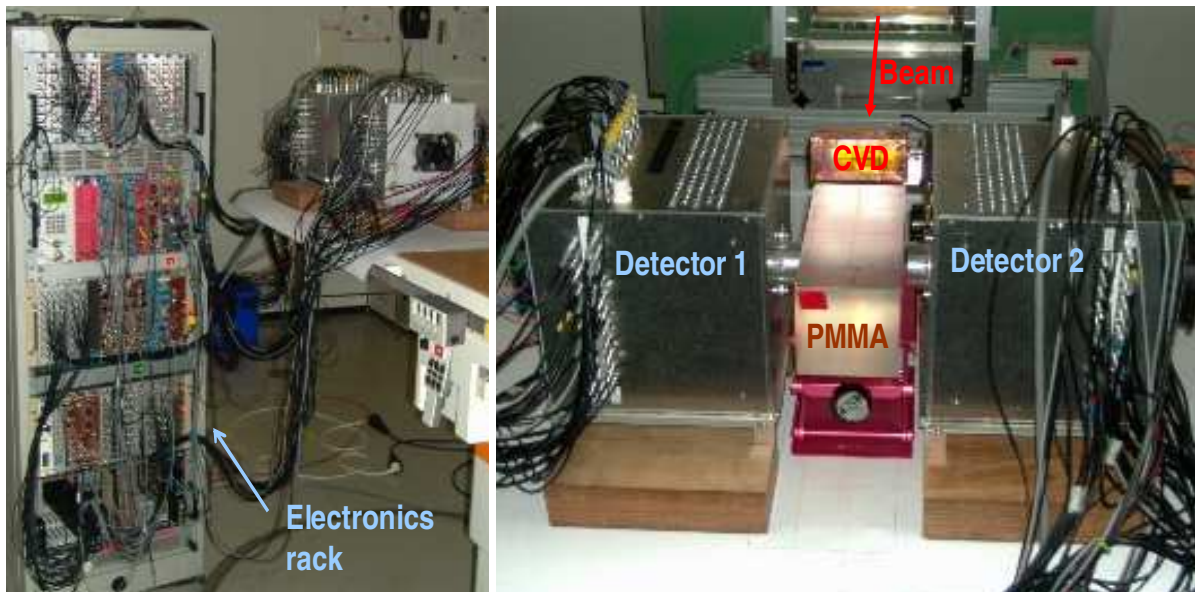
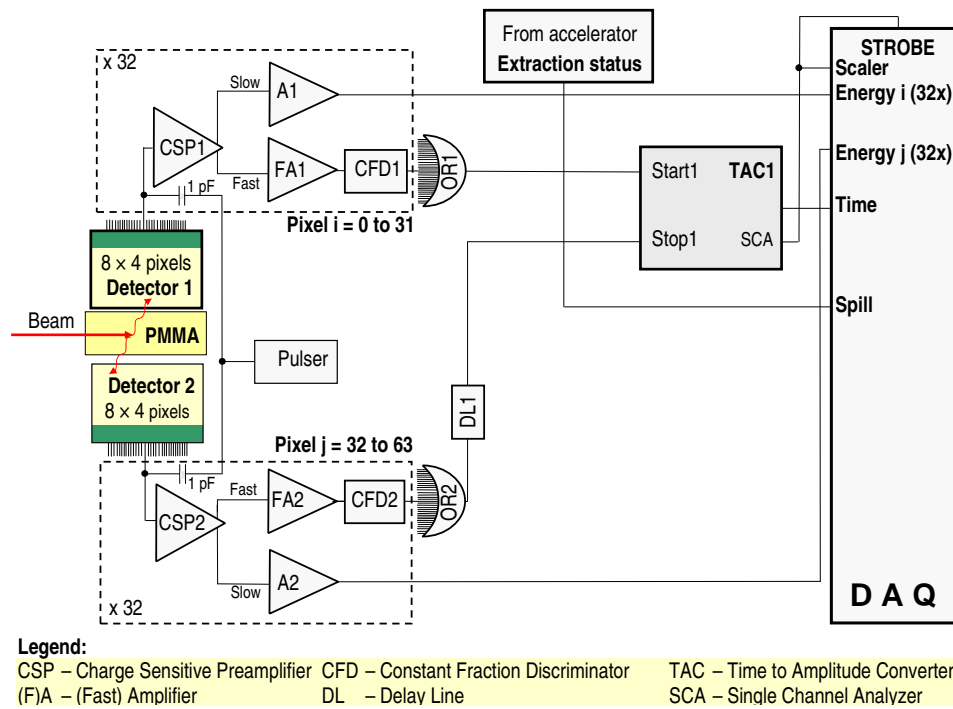


Figure 5.2: Fast-slow coincidence setup for all in-beam imaging experiments. The photographs show the electronics and detector setup positioned at the isocenter of the medical cave at GSI. The chemical vapor deposition diamond detector (CVD, bottom-right) was only used in the experiments described in chapter 6.

slow electronics readout that was implemented. The splitting of the signal from each pixel into a fast (timing) and a slow (energy) shaping electronics chain allowed using conventional, modular nuclear electronics for both time and energy measurements. After splitting the signal at the output of each charge sensitive preamplifier (chapter 4, section 4.5), the slow (energy) signal of each pixel was fed into an 8-input, MA8000 spectroscopy amplifier from Stelzer Physikalische Messgeräte, with $0.5 \mu\text{s}$ shaping constant and adjustable gain ($G \geq 10$). The 64 amplified energy signals were then delivered to four PS7164 CAMAC analog-to-digital converters (ADC) from Phillips Scientific, with 16 inputs each. On the timing chain, each fast signal of each preamplifier was delivered to a PS779 32-channel, fast DC amplifier from Phillips Scientific with gain 10 and, from there, fed into a CF8000 8-input constant fraction discriminator (CFD) from Ortec with 30 ns internal delay. The disjunctively connected outputs of all the CFD of detector 1, implemented with a 429A logic fan-in/fan-out from Lecroy, were then fed into the start input of a TAC/SCA 567 time-to-amplitude converter (TAC) from Ortec, while the disjunctively connected outputs of detector 2 were delayed with an N108 dual delay unit from CAEN to form the TAC stop signal. A time window of about 20 ns was set at the TAC and its single channel analyzer (SCA) digital output gated all CAMAC¹ analog-to-digital converters (ADC) and started the CAGE² data acquisition system (appendix B). The TAC output was fed into an AD811 CAMAC ADC from Ortec.

For every detected coincidence, all 64 energy channels were read, together with the coincidence time between the two detectors and, in addition, one channel containing a digital signal provided by the synchrotron (high for spill on, i.e. beam extraction, ~ 2 s, low for spill off, i.e. pause between extractions, ~ 3 s). This synchrotron signal allows, as necessary during in-beam imaging, to discriminate data acquired during the pauses between the extractions from data acquired during particle extraction. This separation is necessary because of the high background occurring during beam extractions, arising from prompt γ -rays and particles emitted after nuclear reactions between the projectiles and target nuclei (chapter 6). All data generated by each coincidence were recorded in list mode format by means of the data acquisition (DAQ) system described in appendix B. This system also reads a C257 16-input scaler from CAEN that counts all the incoming coincident events, even if not processed by the acquisition electronics, which allows an off-line dead time correction to be performed. Finally, it must be stated that a single pixel threshold was implemented, i.e. an energy threshold of about 250 keV was set individually at each CFD of each pixel. Consequently, the energy spectra present low energy events below the threshold due to noise, interpixel crosstalk and, in the case of spectra acquired during beam extraction, due to the acceptance of low energy events imposed by higher energy events triggering pixels elsewhere in the detectors.

5.3 In-Beam Imaging Performance

This first set of experiments aimed at testing the performance of the detectors under irradiation conditions. Such study was necessary since their imaging capability was expected to be mostly influenced by the particle [Gun04a, Gun04b] and photon [Paw97, Par05b, Cre05d] flux generated by nuclear reactions as the beam penetrates the target.

5.3.1 Setups

The setups depicted in Fig. 5.3 were applied to compare the imaging performance of the detectors when acquiring under and without irradiation of a phantom positioned upstream and downstream from the detectors. The parameters compared were the energy, time and spatial

¹ CAMAC, a backplane electronics bus, stands for computer automated measurement and control.

² CAGE, a C/C++ software/hardware data acquisition solution for CAMAC, stands for CAMAC acquisition through GPIB and ethernet. GPIB stands for general purpose interface bus.

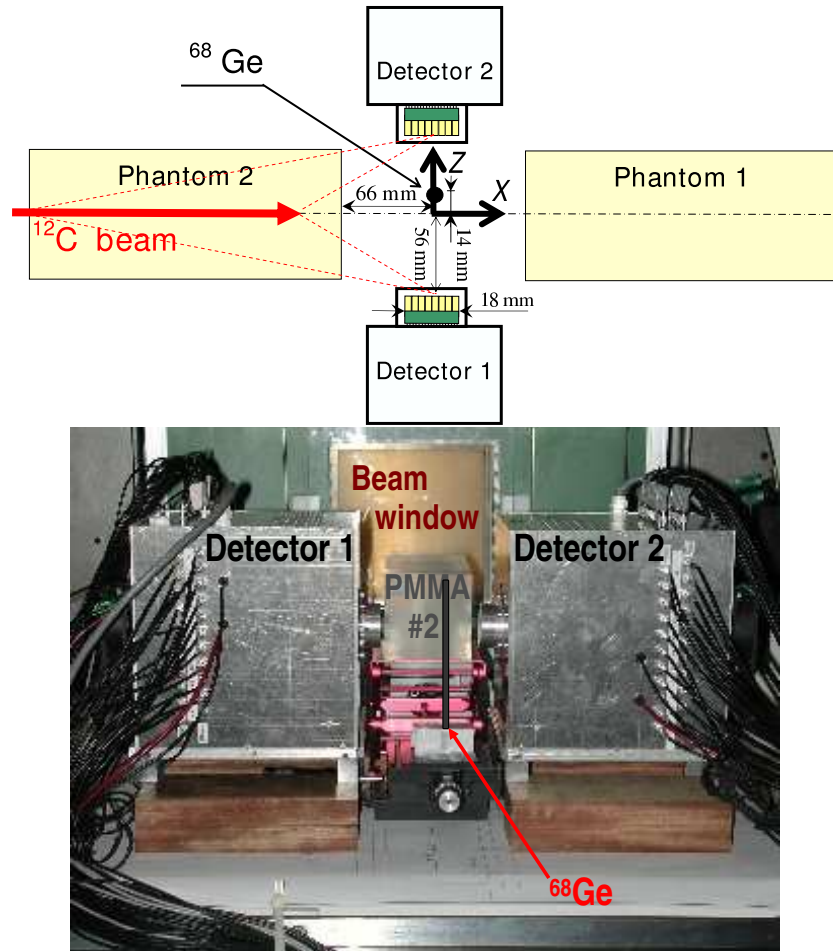


Figure 5.3: Arrangements for the first in-beam PET imaging with LSO/APDA detectors. The photograph shows the setup used for irradiating phantom 2. A ^{68}Ge line source was positioned vertically (along the Y axis), 14 mm apart from the isocentre in order not to be hit during the irradiation. The two phantoms were used alternatively to stop the carbon ion beam upstream (PMMA 2) and downstream (PMMA 1) from the FOV of the detectors.

resolution obtained in each setup. The phantoms were used alternatively and the distances between the irradiated phantom and the detectors were chosen so that the geometry of the edge positioned detectors (dotted circles in Fig. 5.1) of a high acceptance tomograph could be simulated at a scale of approximately 1:3 (Fig. 5.1 versus Fig. 5.3). A ^{68}Ge line source with 3 mm diameter, 14.5 cm length and 17.3 MBq activity was positioned vertically between the detectors, with a shift of 14 mm to detector 2 in order not to be hit by the beam when phantom 1 was used. Imaging of this line source was performed before, during and after the irradiation of the phantoms, each with $9 \times 9 \times 20 \text{ cm}^3$. For that, a pencil-like beam with 3.7 mm diameter (FWHM) and 341.9 AMeV energy penetrated 18.0 cm into each phantom. These were positioned outside the field-of-view (FOV) of the LSO/APDA detectors. The beam intensity was 2×10^8 ions per spill which, after the 1400 spills requested for each irradiation, yields a fluence about 1000 times higher than for a typical daily treatment fraction ($\sim 3 \times 10^8$ ions).

5.3.2 Data acquisition dead-times and event rates

By making use of the accelerator status signal the data acquired could be separated into events collected during beam extractions and during pauses between the beam extractions. The present section summarizes the event rates measured in both regimes after an analysis of the

dead-times η of the data acquisition system (DAQ).

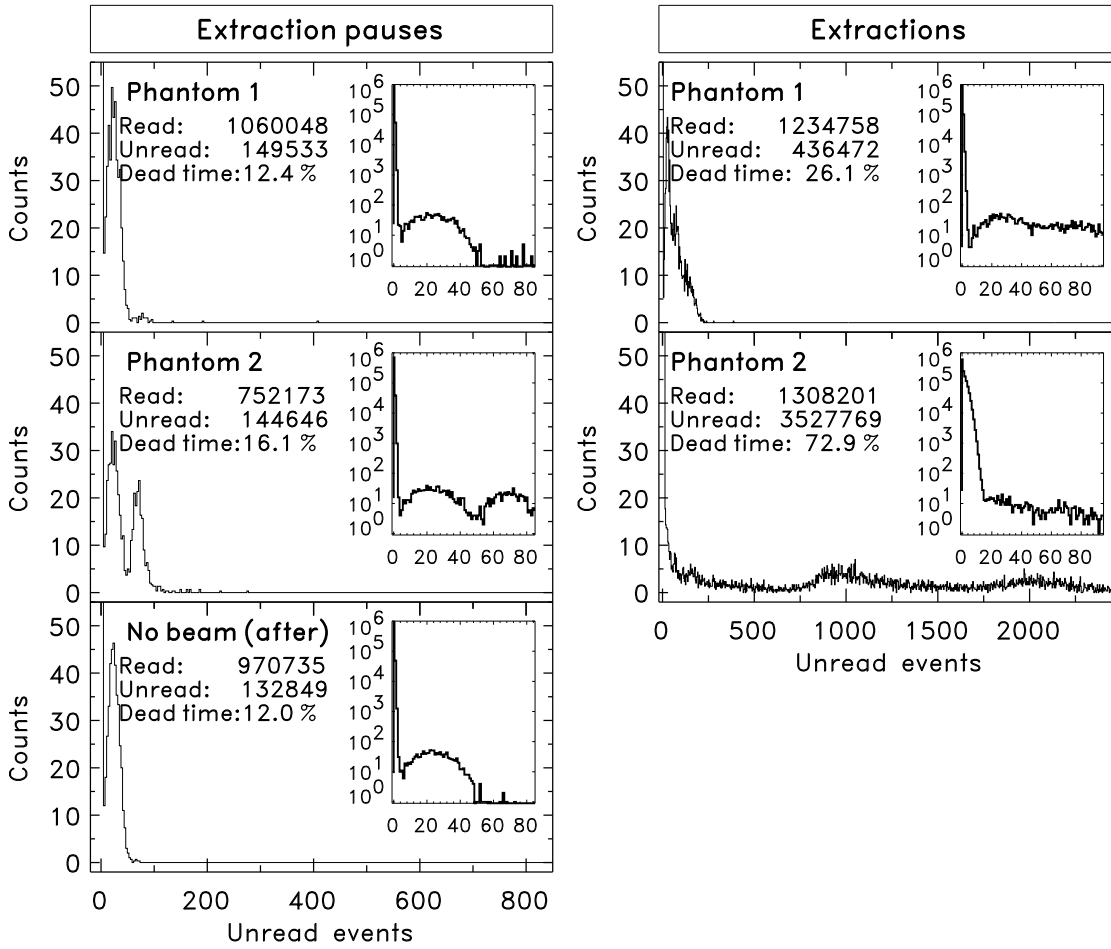


Figure 5.4: Histograms of unread events, with the corresponding data acquisition (DAQ) dead-times, during the extraction pauses and beam extractions.

Fig. 5.4 shows the histograms of unread events obtained during the several imaging setups described in the previous section. The plots were obtained by sampling, from event-to-event, the difference in the scaler values in each event subtracted by unity. That means that the counts in bin 0 correspond to the number of read events where there were no DAQ dead time losses, or the number of counts in bin 20, for example, corresponds to the number of occurrences where 20 events were lost between two consecutive DAQ readouts. The histogram of unread events for the setup without beam, performed before the irradiation of phantoms 1 and 2, is not shown in Fig. 5.4 since it is very similar to the histogram corresponding to the setup without beam but performed after the irradiation of the phantoms (Fig. 5.4, bottom). All histograms of unread events have their maximum at the first bin (unread events = 0, i.e. $\eta = 0\%$) and fall off rapidly from a value above 10^5 to a minimum valley with about 10 counts in bin 10 ($\eta = 90.9\%$), indicating the good performance of the DAQ system with respect to dead time. After bin 10 ($\eta = 90.9\%$), a single peak (double peak for the setup with the detectors positioned downbeam, phantom 2) is observed, corresponding most probably to situations where the data acquisition suffered a buffer overload generating a timeout signal due to the inability of the DAQ system to transfer all its stored events to the acquisition computer in synchronization with the incoming events (appendix B). In such situations an automatic synchronization reset between the several electronics modules driving the acquisition is performed with, consequently,

no data taking during the handshake of the several modules. At all times the scaler implemented continues counting the lost events so that the dead-time can be quantified, as shown in Fig. 5.4. The ratio of events within the first peak in all histograms (bin ≤ 10) to the number of events with bin ≥ 10 is remarkably high, indicating the good capability of the DAQ system to handle the high rates encountered. It must be stated that the input rates handled by CAGE were tested before the experiments to a limit of 100 kcps¹, which was the maximum impulse rate delivered by the pulser available (appendix B). During beam extractions, the extension to higher bins of the histogram of unread events with the detectors positioned downbeam from the irradiated phantom (phantom 2, middle row, right in Fig. 5.4) indicates that the CAGE acquisition system was operating close to its limit in that particular setup, with a high number of buffer overloads generating timeout signals and, consequently, a high number of unread events between readouts.

Table 5.1 summarizes the measured DAQ dead-time η as well the η -corrected event rates. These rates refer to those impinging onto the detectors operated in coincidence and not to the event rate within the FOV of the detectors, i.e. they were calculated taking into account the beam delivery macrostructure for this experiment, namely 2.2 s during beam extractions and 2.3 s during extraction pauses, a time of irradiation of 105 minutes and the DAQ dead-time. No detection efficiency and solid angle corrections were considered at this stage due to the high spatial anisotropy of the incoming events during beam extractions [Gun04a, Gun04b]. A clear asymmetry between the setup with the detectors positioned upbeam and downbeam from the irradiated phantom can be seen, with an event rate about 3 times higher measured with the detectors positioned downbeam from the target.

Table 5.1: Data acquisition dead-times η and event rates measured with the setups of Fig. 5.3.

Experiment	Before irradiation	Detectors up-beam	Detectors down-beam	After irradiation
¹² C beam	No	342.0 AMeV	342.0 AMeV	No
Phantom	No	Phantom 1	Phantom 2	No
$\eta_{extractions}$ (%)	-	26.1	72.9	-
Event rates _{extractions} (cps)	-	542	1570	-
η_{pauses} (%)	11.7	12.4	16.1	12.0
Event rates _{pauses} (cps)	332	376	310	343

cps = counts per second

5.3.3 Energy, time and spatial resolutions during extraction pauses

In the present section the energy, time and spatial resolutions achieved during the extraction pauses are summarized. Fig. 5.5 shows one energy channel and the coincidence time spectrum measured for a ⁶⁸Ge line source placed between the detectors (section 5.3.1). The top row shows the results acquired under irradiation of the phantom positioned downbeam from the detectors, whereas the bottom row shows the results obtained with the phantom irradiated upbeam from the detectors. A slight degradation of the energy resolution during the irradiation with the detectors situated in the forward cone of light nuclear fragments (bottom row, beam stopped in phantom 2) is observed, together with an indication for a slight worsening of the time resolution. The energy and time spectra (not shown) acquired before and after the irradiation of phantoms 1 and 2 are very similar to the spectra acquired during the irradiation of phantom 1 (extraction pauses, Fig. 5.5, top row). The results are evidenced in Table 5.2, which shows

¹ Kilo counts per second (kcps).

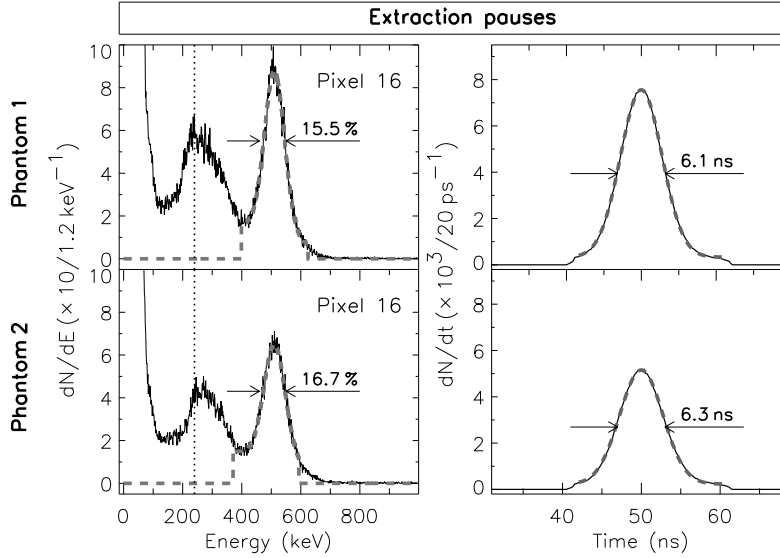


Figure 5.5: Comparison of energy and time resolution measured during the extraction pauses. A ^{68}Ge line source was positioned in the FOV of the two detectors (Fig. 5.3). The beam stopped downstream (top row) and upstream (bottom row) from the detectors. The dotted and dashed lines show the hardware threshold and the Gaussian fit to the full-energy peak, respectively.

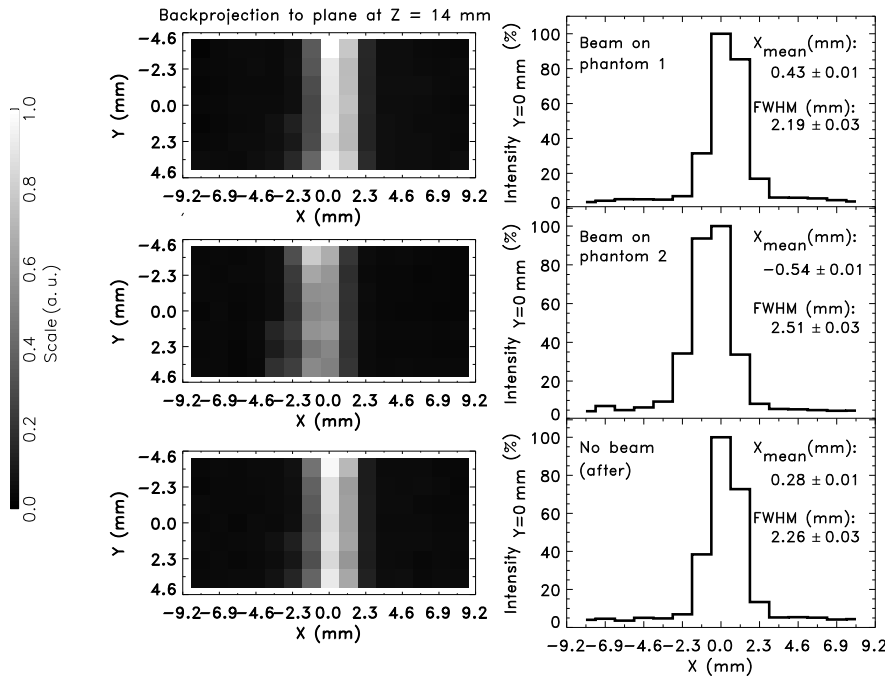


Figure 5.6: Comparison of spatial resolution from in-beam images of a ^{68}Ge line source (Fig. 5.3). The measured datasets were backprojected onto the perpendicular plane between the detectors at $Z = 14$ mm (left column). The images in the right column show the normalized linear profiles through the middle of the backprojected plane on the left column.

both the mean energy resolution for all 64 channels as well as the coincidence time resolution obtained in all measurements with the ^{68}Ge line source.

In Fig. 5.6 it can be seen that the spatial resolution is also slightly worsened for the detectors

Table 5.2: Imaging a ^{68}Ge line source (setup of Fig. 5.3).

Experiment	Before irradiation	Detectors up-beam	Detectors down-beam	After irradiation
^{12}C beam	No	342.0 AMeV	342.0 AMeV	No
Phantom	No	Phantom 1	Phantom 2	No
$\Delta E/E$ (FWHM, %)	15.5 ± 0.5	15.5 ± 0.3	16.4 ± 0.6	15.5 ± 0.3
Δt (FWHM, ns)	6.2 ± 0.2	6.1 ± 0.2	6.3 ± 0.2	6.2 ± 0.2

positioned in the forward cone of the stopped beam. The images of the line source obtained before any phantom irradiation are not shown in Fig. 5.6. They are very similar to those obtained after the irradiation. The backprojection onto the plane between the detectors containing the ^{68}Ge line source is shown and allows to see a slightly worse spatial resolution, quantified for the linear profile of the line source. More importantly, in all the in-beam experiments it has been observed that after finishing the irradiation the time, energy and the spatial resolution returned back to the initial values.

5.3.4 Energy and time spectra during beam extractions

The analysis of the energy and time spectra measured during beam extractions clearly reveals a much higher random contamination for the detectors positioned downstream from the beam stopping region. Fig. 5.7 shows energy and time spectra collected for the two setups stopping the beam in Fig. 5.3. In the energy spectra corresponding to the setup of phantom 1 a drop in the number of events below the hardware threshold is observed, as shown for pixel 16 in Fig 5.7. This behaviour, described in section 5.2, is expected due to the lower count rates measured in this configuration (Table 5.1). In the setup receiving higher event rates (phantom 2, bottom row) no discontinuity is observed at the threshold value due to the increased background events

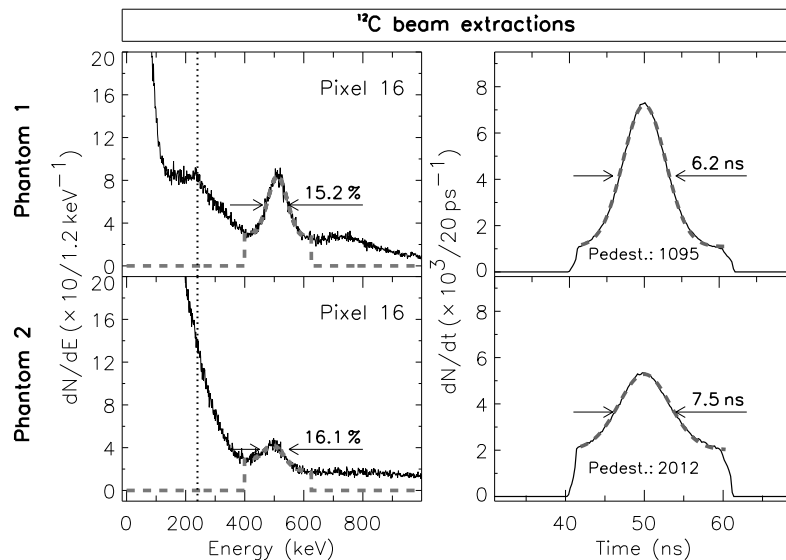


Figure 5.7: Energy and time spectra obtained during beam extractions. A ^{68}Ge line source was positioned in the FOV of the two detectors (Fig. 5.3). Results show the beam stopped downstream (top row) and upstream (bottom row) from the detectors. The dotted and dashed lines show the hardware threshold and the Gaussian fit to the full-energy peak, respectively.

being imaged. Fig. 5.7 shows clearly that in the setup with the detectors positioned downstream from the irradiation (phantom 2) a much higher background is present, resulting in a lower height of the 511 keV peak and worse energy resolution. In addition, the time spectrum also shows a resolution deterioration, with a twofold increase in the pedestal value revealing the presence of a higher number of random events. For the present experiments a separation of the events collected during beam extractions and during the extraction pauses was enough to image successfully the ^{68}Ge line source positioned in the FOV of the detectors. But this high event yield must be further carefully studied if in-beam PET imaging during beam extractions will be implemented, as necessary for future heavy ion therapy installations, where a higher accelerator duty factor in comparison to the GSI medical machine is expected (chapter 6).

5.4 Imaging ^{12}C Beam Induced Positron Emitter Distributions

This set of experiments was devoted to the imaging of the positron emitter depth distribution generated by a pencil-like ^{12}C beam stopping in a phantom. Such an imaging experiment is of importance since it simulates the application of the detectors under study for monitoring the ^{12}C patient tumor irradiation. These β^+ activity measurements check, furthermore, the imaging capability of the detectors after being exposed to the irradiation of two phantoms with high fluences (about 1000 times higher than for a typical daily treatment fraction) and with the detectors positioned up and downbeam from the irradiated phantom.

5.4.1 Setup

As shown in Fig. 5.8, the FOV of the longitudinal positron camera formed by the two detectors is much smaller than the beam range in PMMA (18 mm versus 74 mm, respectively, with a beam energy of 200.3 AMeV). Therefore, the phantom ($9 \times 9 \times 20 \text{ cm}^3$) was moved through the FOV in 9 steps of 9 mm each (half the axial length of one LSO/APDA detector), thus

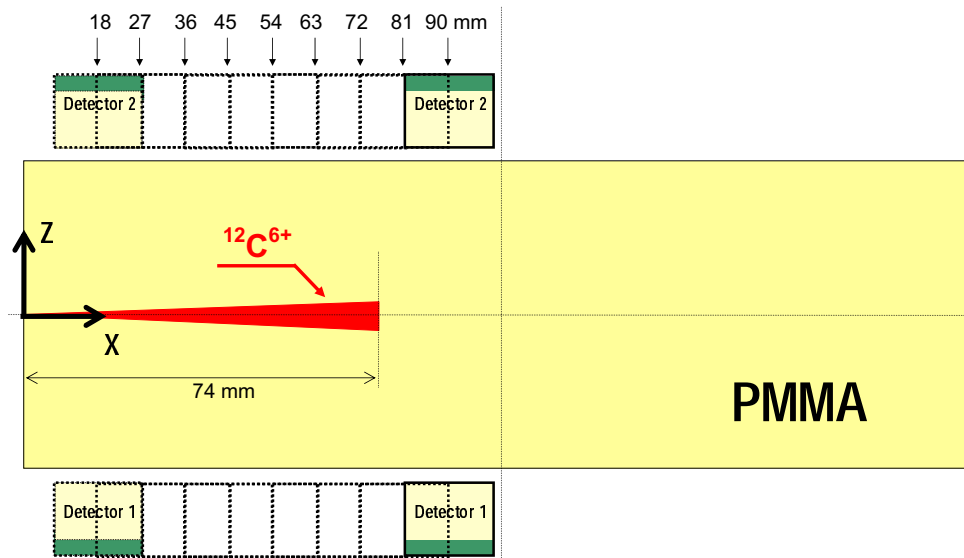


Figure 5.8: Arrangement for the second set of in-beam PET imaging experiments. Nine phantoms were irradiated subsequently in order to image the β^+ activity resulting from stopping the carbon ion beam. The position of the centre of the detectors relative to the front face of each phantom is shown by the arrows at the top.

covering 99 mm parallel to the beam track (Fig. 5.8). For each detector position one new phantom was used in order to avoid the remaining activity from the previous irradiation to be detected. The photograph in Fig. 5.2 shows one such phantom exactly positioned between the LSO/APDA detectors. The chemical vapor deposition (CVD) diamond particle detector shown in the photograph was not used at this stage, but at a later stage for implementing random suppression during beam extractions, described in chapter 6.

5.4.2 Data acquisition dead-times and event rates

In order to perform quantitative imaging of the ^{12}C beam induced positron emitter distribution, presented in the next section, three items must be known: the solid angle of the FOV formed by the two detectors, the overall photon detection efficiency and the acquisition dead time η . This section evaluates the latter, divided into $\eta_{\text{extractions}}$ and η_{pauses} . Fig. 5.9 shows the histograms of unread events obtained for the whole scan described in section 5.4.1. The corresponding DAQ dead-times are also shown. By considering both the beam delivery macrostructure for the used ion energy, with beam extractions taking 2 s and extraction pauses 3 s, as well as the irradiation time of 20 minutes, the mean coincidence event rate impinging onto the detectors and forming a signal above threshold in both detectors could be calculated, yielding 20 cps and 652 cps during extraction pauses and beam extractions, respectively.

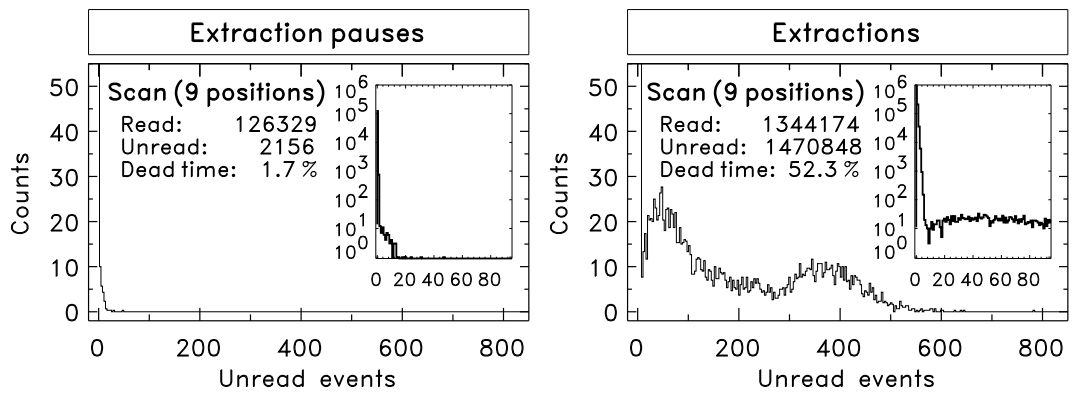


Figure 5.9: Histograms of unread events, with the corresponding data acquisition (DAQ) dead-times, during the scanned measurements depicted in Fig 5.8.

5.4.3 Depth-profile and 2D longitudinal tomogram

Fig. 5.10 shows the measured β^+ -activity distribution obtained by shifting the irradiated phantoms along the beam direction, as described in section 5.4.1. Both the depth-profile and the longitudinal tomogram were obtained by backprojecting the coincidence data onto the central plane between the detectors. Only events leaving a signal within an energy window of 300 to 850 keV in the triggered pixels of both detectors were selected.

The shape of the measured distribution is in agreement with the expectations from the kinematics of the nuclear fragmentation reactions leading to the positron emitters [Eng92]. Onto a plateau of activity formed by target fragments (^{11}C , ^{10}C , ^{15}O and ^{13}N), a pronounced activity maximum due to the projectile fragments (^{11}C , ^{10}C) is superimposed (Fig. 1.17).

For quantification of the image acquired during the extraction pauses, the parameters shown in Table 5.3 were used, namely the DAQ dead time η_{pauses} , the geometrical solid angle at the image center Ω_{\odot} , the image fill factor Π , described in section 4.6.2, the probability for escape

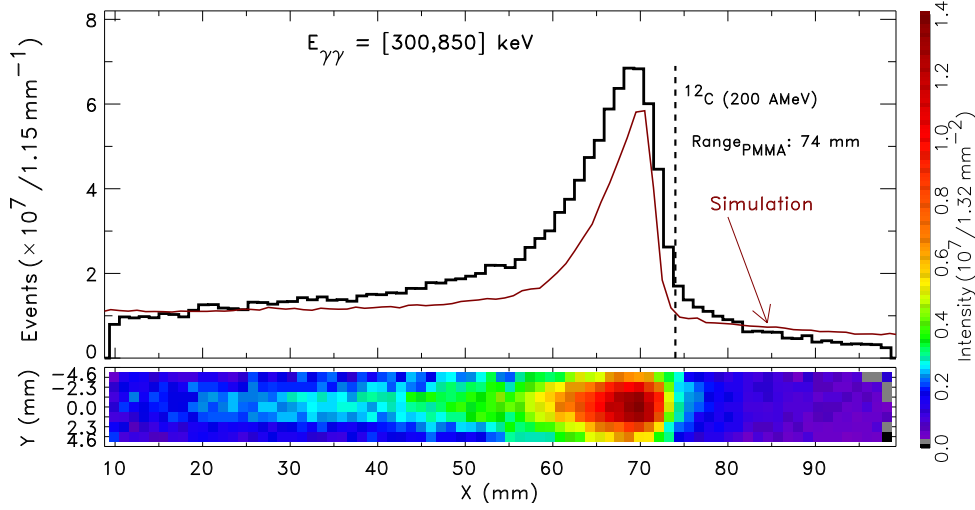


Figure 5.10: Depth-profile and longitudinal tomogram of the β^+ activity induced by stopping the carbon beam within the field of view (FOV) of the LSO/APDA detectors.

of the two unscattered annihilation γ -rays from the phantom, $P_{\gamma\gamma\text{esc}}$, and the efficiency for detecting a photon coincidence in two opposing LSO crystals within the considered energy window ε'_{LOR} .

Table 5.3: Parameters used for image quantification (extraction pauses).

Name	Symbol	Value
Detected coincidences	N_d	87705
Dead time	η_{pauses}	1.7 %
Solid angle (32 LOR)	$\Omega_{\odot} = 32 \cdot \Omega_{LOR}$	$32 \cdot 2.3 \times 10^{-4}$
Image fill factor	Π	30.5 %
Double γ -ray escape from phantom	$P_{\gamma\gamma\text{esc}}$	15.2 %
LOR efficiency (photopeak, no phantom)	ε_{LOR}	4.9 % (Eq. 4.11)
LOR efficiency (300 to 850 keV, no phantom)	ε'_{LOR}	$3.7 \cdot \varepsilon_{LOR}$
Corrected coincidences	N_c	1.44×10^9
Expected coincidences	N_e	1.41×10^9

The value of η_{pauses} was presented in section 5.4.2. To obtain Ω_{LOR} a simulation routine similar to that described in section 4.6.3 was written. This routine considered 10 million events at the isocenter annihilating isotropically and counted those events impinging onto the surfaces of two opposing pixels. The overall geometrical solid angle at the isocenter Ω_{\odot} follows by multiplication with the number of LOR (32). This method was preferred instead of taking into account the full frontal area of the LSO matrix detectors because of the non-negligible dead area surrounding each LSO crystal. This area is filled with air and teflon tape. In order to account for the smaller geometrical solid angle of image voxels positioned elsewhere than the isocenter, the flood source measurement with exactly the same detector geometry, studied in section 4.6.2, was used to correct on a voxel-by-voxel base the number of events backprojected into the mid-plane image. This correction represents the mean relative geometrical solid angle of each image voxel with respect to the central one and is given by the mean image fill factor Π , defined in section 4.6.2. Since neither Ω_{\odot} nor Π account for the absorption of photons in the phantom, the probability for escape of the two unscattered annihilation γ -rays from the phantom, $P_{\gamma\gamma\text{esc}}$, was

calculated based on the absorption value for 511 keV photons in PMMA ($9.32 \times 10^{-2} \text{ cm}^2 \text{ g}^{-1}$, with $\rho_{PMMA} = 1.18 \text{ g cm}^{-3}$) obtained from [Xco99]. The efficiency for detecting a photon coincidence in two opposing LSO crystals with photon energy values between 300 and 850 keV (ϵ_{LOR}) was measured to be 3.7 times higher than the same efficiency calculated for two photons with energy values lying within the FWHM of the photopeaks (Table 4.2).

The simulation of the expected number of counts N_e was achieved with the PosGen Monte-Carlo code [Has96, Pön04], with its output confirmed in appendix C. The code yields a total of 1.98×10^7 β^+ -decaying nuclei produced per each spill with 2×10^8 carbon ions with 200.2 AMeV energy. The expected total number of counts $C^{(j)}$ from the decay of isotope j with half-life $T_{1/2}^{(j)}$ followed by integrating the initial activity $A_0^{(j)}$, induced per spill, over the 240 spills used (5 s spill period):

$$C^{(j)} = A_0^{(j)} \frac{T_{1/2}^{(j)}}{\ln 2} \sum_{i=0}^{239} \left[1 - \exp\left(\frac{-i \cdot 5 \text{ s}}{T_{1/2}^{(j)} / \ln 2}\right) \right]. \quad (5.1)$$

The simulation curve in Fig. 5.10 regards acquisitions in the extraction pauses and, consequently, considers only isotopes with half-lives larger than a second (^{11}C , ^{10}C , ^{15}O and ^{13}N) weighted with the timing fraction of the extraction pauses: 3/5, so that

$$N_e = \frac{3}{5} \cdot \left[\sum_j C^{(j)} - C_{8.8 \text{ mm}}^{(j)} \right], \quad j = ^{11}\text{C}, ^{10}\text{C}, ^{15}\text{O}, ^{13}\text{N}, \quad (5.2)$$

with $C_{8.8 \text{ mm}}^{(j)}$ being the number of coincidences expected to have been measured if the phantom length between 0 and 8.8 mm would have been imaged (cf. Figs. 5.8 and 5.10). By taking into account the irradiation time of 1200 s, a beam penetration depth of 65 mm and its circular, Gaussian cross section with 1 cm FWHM¹, the measured β^+ -activity density created by the incoming carbon ion fluence amounts to $5.3 \times 10^5 \text{ Bq cm}^{-3}$. This corresponds to 98 and 350 $\text{Bq cm}^{-3} \text{ Gy}^{-1}$ if the maximum and average² dose of 5.4 kGy and 1.5 kGy, respectively, is considered.

5.5 LSO Activation Studies

The pioneering work at the Lawrence Berkeley National Laboratory (LBNL) between 1971 and 1992 [Pet94], where the first steps towards using heavy ions for radiotherapy were done (section 1.2.3), included a great amount of research with positron emission tomography [Tob71, Tob77, Lla88]. Nevertheless, the clinical implementation of in-beam PET had to be abandoned at LBL since the scintillator material (BGO) was activated. The reason for this was assumed to arise from the light particles produced by the use of passive beam shaping [Lla88]. At GSI, the use of the raster-scan technique [Hab93] made possible the successful implementation [Paw97] and clinical use [Eng04b] of the in-beam positron tomograph BASTEI (chapter 1, section 1.4.2). With the studies summarized in chapter 2 indicating a great improvement in the quality of in-beam PET images if the gap between the dual-head tomograph is made smaller, it became important to study whether the scintillator material for the next-generation in-beam PET detector (LSO) becomes activated by the flux of light particles leaving the patient downbeam [Gun04a, Gun04b].

¹ For the dose calculation the beam cross section is given by $\pi\sigma^2$, with $\sigma = \text{FWHM}/2.35$.

² Calculated between 0.9 and 8 cm with the PosGen code.

5.5.1 Method

In order to maximize the amount of particles hitting the scintillators under study, two patients with only one irradiation portal were selected. A small matrix of nine LSO crystals with a total volume of about 0.6 cm^3 was placed at their masks downbeam, following the beam direction with maximum penetration depth in order to meet the expected maximum light particle flux leaving the irradiated patient. Fig. 5.11 depicts the positioning of the irradiated LSO crystals

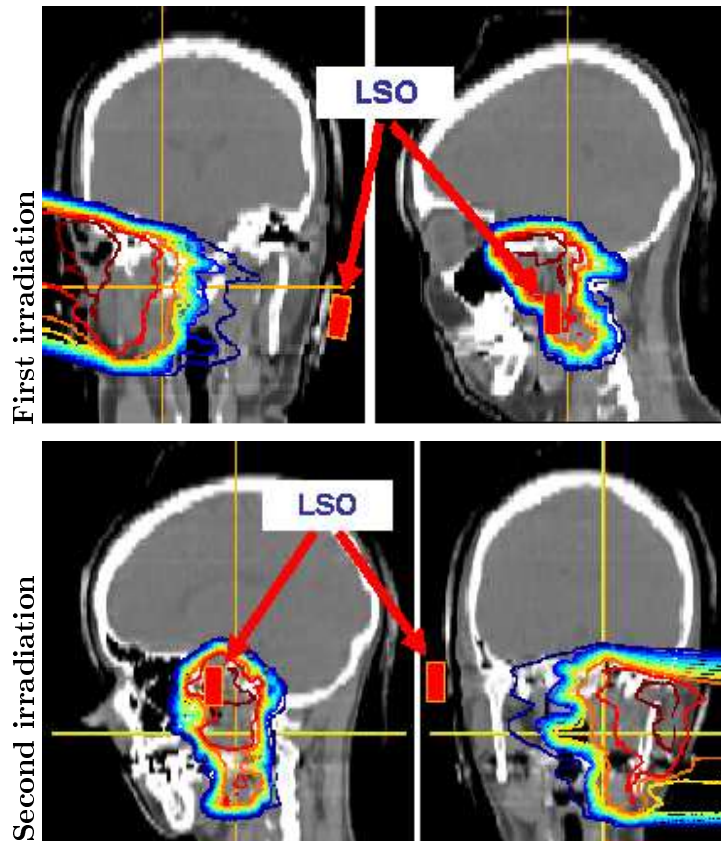


Figure 5.11: Dose distributions (frontal and sagittal views) of the two single-portal treatments in the skull base showing the irradiated LSO outside the masks. The dose distributions, plotted with iso-dose lines from 5 % (dark blue) to 95 % (red) of the maximum dose, are overlaid on the patient CT (grey image).

outside both patient masks. The maximum dose imparted in the field of the first irradiated patient was 1.02 Gy delivered with 1.23×10^9 ^{12}C ions with energies ranging from 126 to 258 AMeV. The second patient received a fluence of 1.29×10^9 ^{12}C ions with 113 to 255 AMeV, corresponding to a dose maximum of 1.05 Gy.

5.5.2 High-resolution γ -ray spectra and their interpretation

Spectroscopic measurements of the irradiated crystals, performed with a high-purity germanium (HPGe) detector, were compared with measured spectra acquired before the irradiation (one overnight measurement was made before the crystals were irradiated). The spectroscopic measurement of the irradiated crystals started approximately 2 minutes after finishing the dose delivery to the second patient. The spectrum was saved after 1, 2, 4, 8, 16, 45 minutes and after 4 hours and 21 minutes. Finally, several measurements of 6 hours each were taken during

the following 4 days. Figs. 5.12 and 5.13 show the spectra obtained. The top spectrum in each row shows the overnight measurement sampled before irradiating the crystals (53 800 s). The bottom spectrum in each row was started 2 minutes after the crystals were irradiated and acquired during 15 700 s. When evaluating the photon lines shown, only peak heights greater or equal than 3σ above the background were considered. In order to attribute the energy values to the lines found the HPGe detector had been previously calibrated (Deutscher Kalibrierdienst DKD) with a radioactive homogeneous mixture and the corresponding calibration files were used (energy only). Since the calibration source (1 liter volume with 1 g cm^{-3} density) did not have the same shape and density as the crystal matrix, the efficiency calibration could not be used and, consequently, a quantitative analysis (number of decays in the crystal matrix itself) was not possible. Nevertheless, the crystals were positioned in exactly the same position before and after the irradiation so the comparison of the corresponding spectra in quantitative terms is valid. For isotope identification both the table of isotopes [Fir96] as well as its database available online [TOI04] were used.

Natural decay chains from ^{232}Th and ^{238}U

The comparison of the lines present before and after irradiating the crystals shows some peak enhancement for selected energies. In order to quantify this enhancement the count rates at the detector were calculated by considering, for each line in each measurement, the peak area above the background level. Fig. 5.14 shows two stable (top) and two enhanced (bottom) γ -ray lines which were identified to arise from the decay of isotopes belonging to the natural decay chains of ^{232}Th and ^{238}U , respectively (Fig. 5.15).

The reason for the different behaviour of the two natural decay chains lies on the presence of ^{222}Rn , a gas at normal pressure and temperature, in the ^{238}U series. While the ^{232}Th series shows no sign of activity enhancement (Fig. 5.14, top), the bottom images clearly show an increase in count rate after the measurement performed after the crystal matrix irradiation was started. It is a known fact that the presence of ^{222}Rn and its decay products constitutes a major part of airborne radioactivity [Par77]. This gaseous element must have drifted into the container surrounding the HPGe detector, which was not totally closed to the atmosphere. More importantly, the removal and later re-introduction of the crystal matrix after the irradiation changed the air conditions in the measuring container. Due to this dynamic behaviour, the decay curves shown in the bottom images of Fig. 5.14, despite clearly showing an increase in activity in respect to the activity value registered before irradiating the crystals, do not exhibit the typical decrease of activity proportional to the lifetime of the original element.

Decay of ^{176}Lu into ^{176}Hf and the 511 keV line

Fig. 5.16 shows two γ -ray lines characteristic of the decay of ^{176}Lu to ^{176}Hf . As it can be seen, no activity enhancement significantly above the measured error bars is observed. More importantly, no new γ -ray lines arise at an energy equal or close to 511 keV (Fig. 5.12) thus, from the point of view of LSO activation, the flux of particles leaving the patient downbeam do not pose a problem to in-beam PET imaging even for the detectors positioned at small angles with respect to the beam direction.

5.6 Influence of the Natural Radioactivity of LSO

Despite its many advantages as a scintillator for PET, the lutetium in LSO contains approximately 2.6 % ^{176}Lu , a naturally occurring radioisotope with a half-life in the order of 3.8×10^{10} years. The decay of ^{176}Lu leads to a measured background rate density of ap-

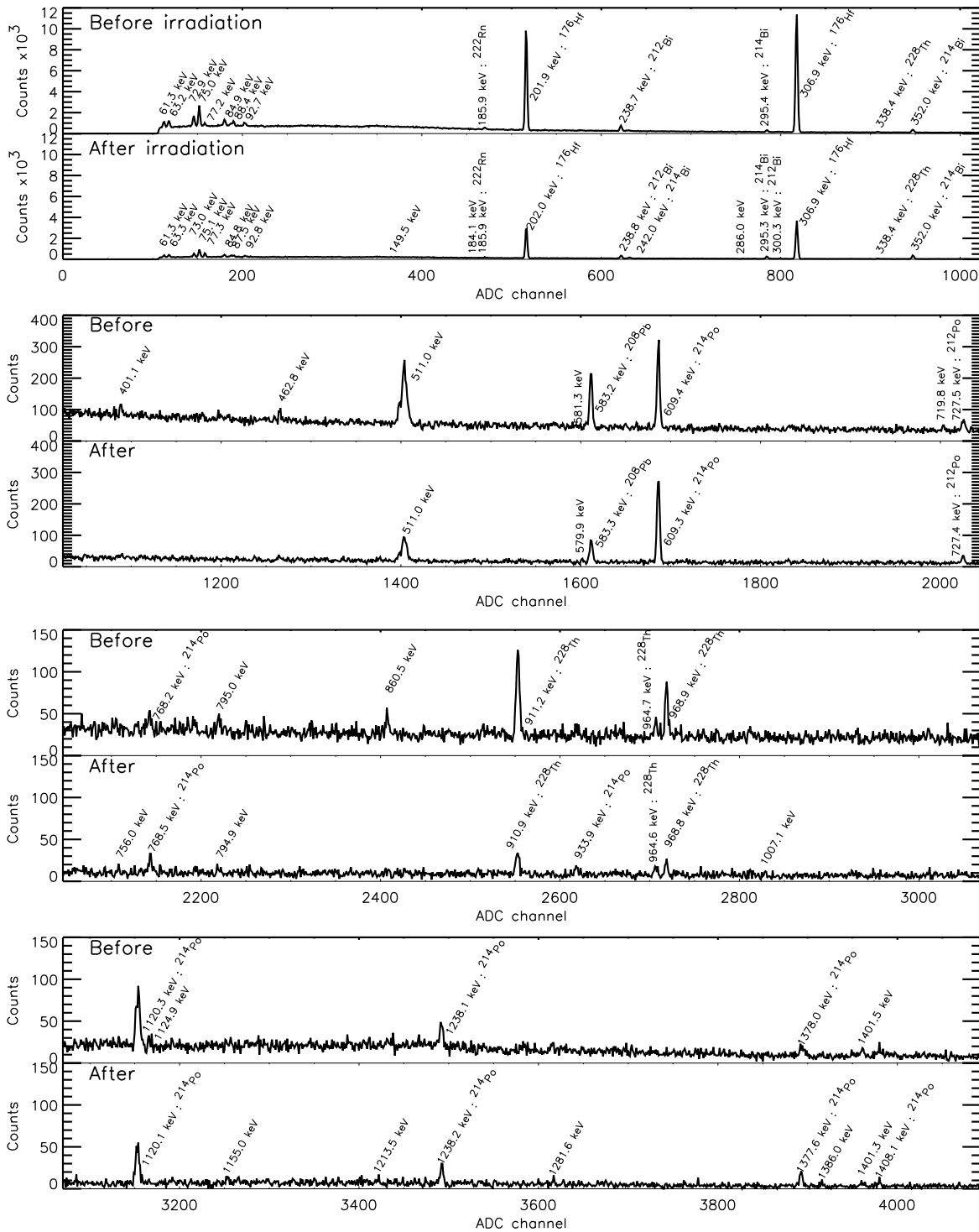


Figure 5.12: LSO activation studies with a high purity germanium (HPGe) detector. Spectra show lines of lower energy. The acquisition times are 53 800 s and 15 700 s for the spectrum measured before and after the crystal irradiation, respectively.

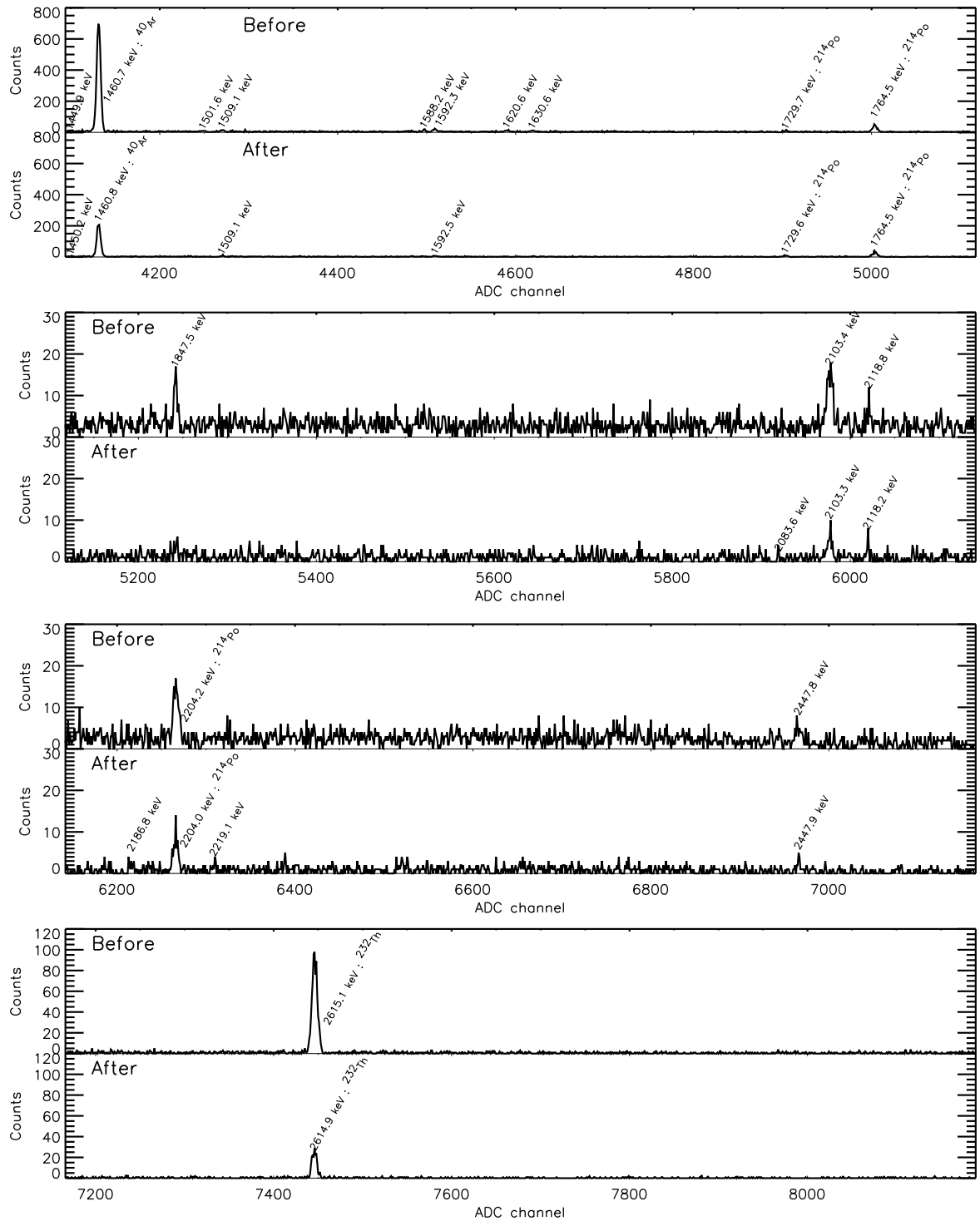


Figure 5.13: LSO activation studies with a high purity germanium (HPGe) detector. Spectra show lines of higher energy. The acquisition times are 53 800 s and 15 700 s for the spectrum measured before and after the crystal irradiation, respectively.

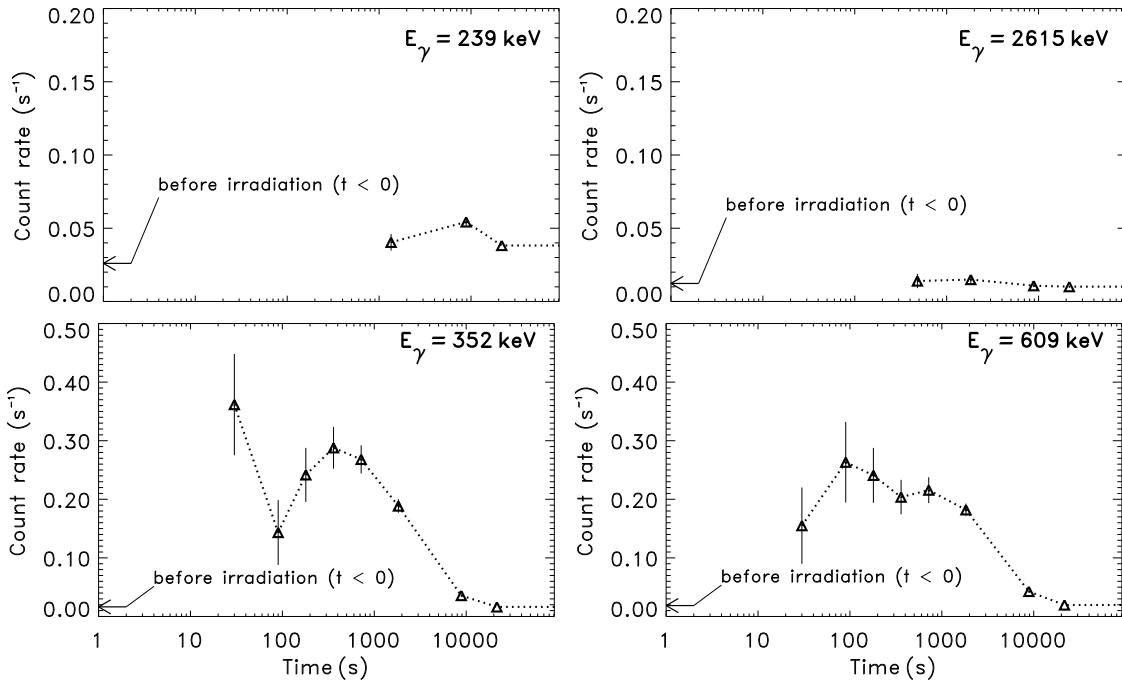


Figure 5.14: Count rates from the two stronger γ -ray lines from the ^{232}Th (top) and ^{238}U (bottom) series.

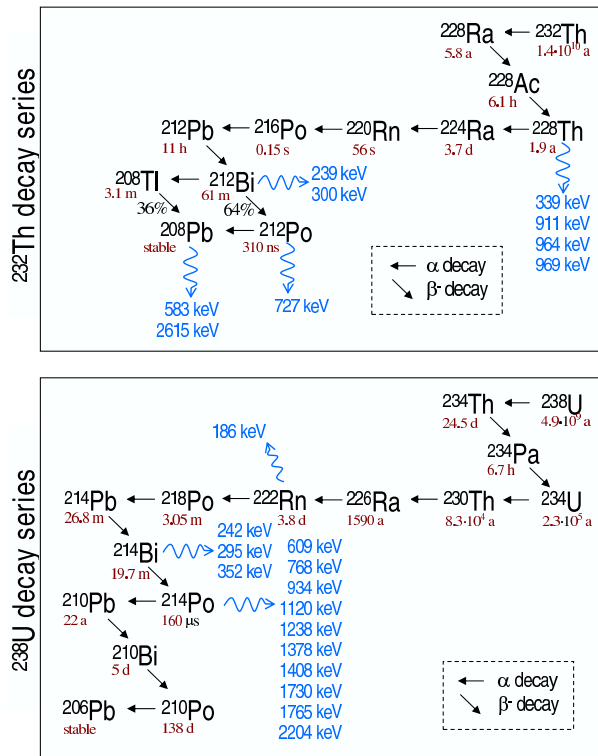


Figure 5.15: Decay chains of the natural elements ^{232}Th (top) and ^{238}U (bottom), with the half lives of each isotope shown below it.

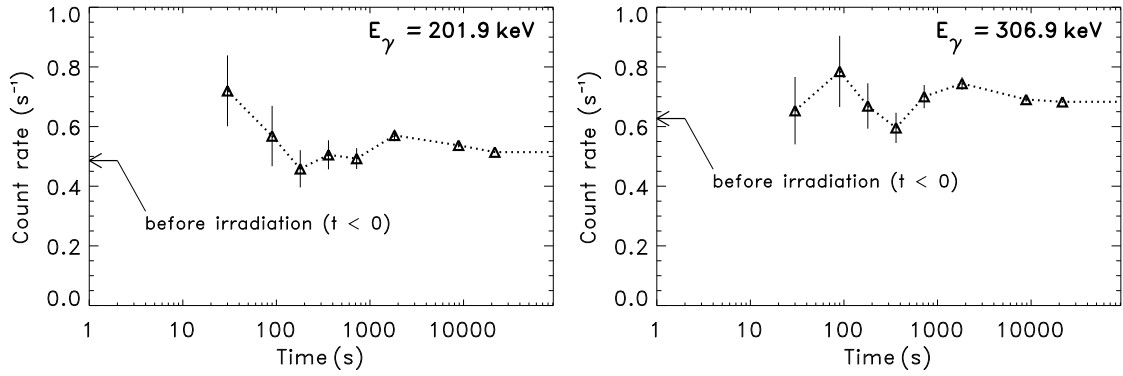


Figure 5.16: Count rates from two γ -ray lines from the decay of ^{176}Lu to ^{176}Hf .

proximately 240 Bq cm^{-3} of scintillator material [Hub02]. Its decay scheme is shown in Fig. 5.17, together with the resulting natural radioactivity measured in an LSO crystal with $10.5 \times 10.7 \times 13.7 \text{ mm}^3$ [Hub02]. Also shown is the kinetic energy spectrum of the β^- -decay, calculated with a non-relativistic approximation according to [Mar66].

The shape of the background spectrum from LSO is thought to arise from γ -ray absorption within the crystal itself, mostly by photoabsorption but also by Compton scattering. This results in a shift to higher energies of the background spectrum in respect to the β^- energy curve. The peak at approximately 700 keV results most probably from the simultaneous detection of the β^- particle, with a most probable energy value of about 400 keV, as shown, together with the γ -lines with energies of 202 and 88 keV.

In order to estimate the random coincidence rate expected with the LSO/APDA detectors two energy windows typically installed in PET systems were considered and are depicted in Fig. 5.17 with vertical lines. These are 400-600 keV (dot-dashed) and 350-650 keV (dotted), corresponding to a selection of events within $511 \text{ keV} \pm 17\%$ and $511 \text{ keV} \pm 27\%$, respectively. Within the narrower energy window the activity density is 66 cps cm^{-3} , whereas the wider energy window yields 97 cps cm^{-3} .

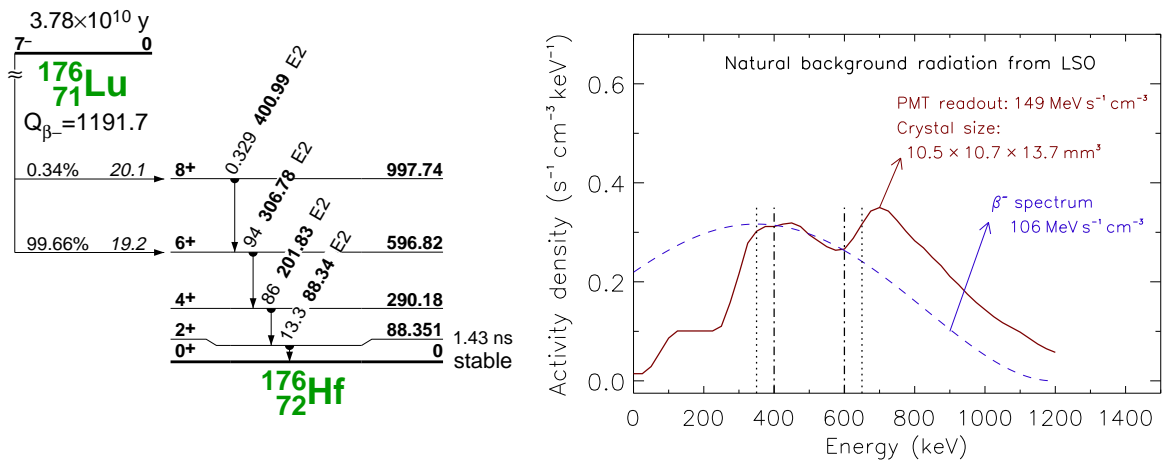


Figure 5.17: Decay scheme of ^{176}Lu into ^{176}Hf by β^- emission (left), taken from [Fir96], and measured natural radioactivity from LSO (right), taken from [Hub02]. Also shown is the calculated kinetic energy spectrum of the β^- -decay.

5.6.1 Extrinsic and intrinsic true and random coincidences

The random coincidence rate R_i that results from the activity density calculated in the previous section arises from the intrinsic activity of LSO. In a PET measurement, the total random coincidence rate is the sum of R_i with the extrinsic random coincidence rate R_e , with R_e arising from the physics processes inherent to the sampling of annihilation radiation. Fig. 5.18 illustrates the contribution of the intrinsic and extrinsic event rates to both the true and the random rates measurable in an LSO-based PET scanner.

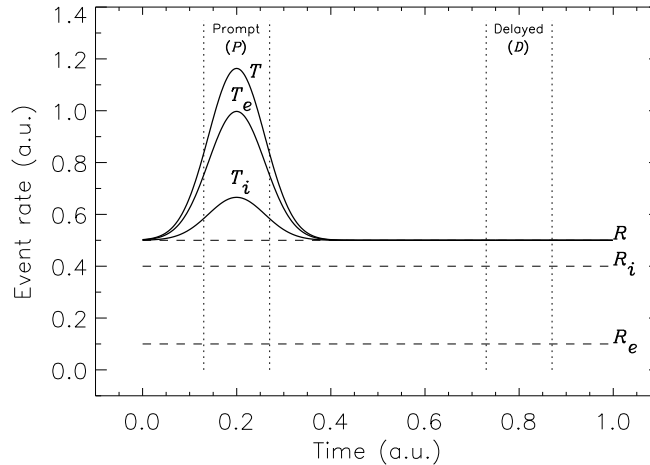


Figure 5.18: Illustration of the intrinsic and extrinsic true and random coincidence rates in LSO-based PET scanners. The intrinsic contribution arises from the natural radioactivity of LSO and is fixed for a given tomograph. It can be quantified with a simple blank scan. The extrinsic rates depend on the intensity and geometrical distribution of the β^+ activity being measured.

The prompt P and delayed D time windows plotted in Fig. 5.18 with vertical dotted lines represent the basis of the so-called delayed coincidence random suppression method, currently implemented in most modern PET scanners [Bad96]. In summary, this method calculates the true event rate T occurring in each LOR by subtracting D from P , with D being the event rate measured in a time window arbitrarily delayed in respect to the prompt coincidence time window. For random coincidence rates stationary in time $D = R$. The intrinsic true coincidence rate T_i shown in Fig. 5.18 arises from events where a ^{176}Lu nuclide undergoes β^- -decay in one detector and emits a prompt γ -ray that is absorbed in a second detector.

The delayed coincidence random suppression method is sufficient for PET systems without intrinsic detector radioactivity or for PET measurements where the intrinsic detector radioactivity is much smaller than the signal activity being sampled [Wat04]. For in-beam PET, though, the measured activity density lies orders of magnitude below that sampled in human PET studies (section 6.1) and a detailed analysis of both T_i and R_i is necessary in order to compare their values with the expected in-beam PET signal T_e at future planned tomographs. The influence of T_i onto realistic in-beam PET images acquired with BASTEI was studied in [Lau00] by assuming the BGO material substituted with LSO in that tomograph. In the following section that study is complemented by calculating the value of T_i expected for a closed-ring and a dual-head tomograph with narrow gaps (Fig. 5.1), and extended by comparing the expected intrinsic random coincidence rate R_i with the in-beam PET signal T_e .

5.6.2 Extrapolation to tomographs with intrinsic radioactivity

Influence of the intrinsic random coincidence rate R_i

The influence of the measured natural background from LSO on the PET images obtained by a given tomograph can be quantified by means of the so-called randoms-to-trues ratio RTR [Wat04]. In the present background considerations the RTR measured in a given LOR between two opposed pixels of a tomograph is given by

$$RTR = \frac{R_i}{T_e} = \frac{2 \Delta t (a_i V_{pix})^2}{a_e V_{vox} \Omega_{vox} P_{\gamma\gamma esc} \epsilon_{scint}^2 \epsilon_{ph}^2}, \quad (5.3)$$

with symbols and values defined in Table 5.4. An intrinsic activity density a_i of 66 Bq cm^{-3} , expected for an energy window from 400 to 600 keV (section 5.6), was considered.

Table 5.4: Parameters for quantifying the randoms-to-trues ratio RTR in an LSO-based tomograph with 45 cm inner radius.

	Name	Symbol	Value	Unit
R_i	Coincidence time resolution	$2 \Delta t$	4	ns
	Intrinsic activity density ^a	a_i	66^a	Bq cm^{-3}
	Volume of pixel looking at LOR	V_{pix}	$1 \times 1 \times \text{crystal depth}$	cm^3
T_e	Extrinsic activity density (PET signal) ^b	a_e	200^b	$\text{Bq cm}^{-3} \text{ Gy}^{-1}$
	Volume of image voxel	V_{vox}	$1 \times 1 \times 1$	cm^3
	Double γ -ray escape from object	$P_{\gamma\gamma esc}$	not considered	
	Solid angle of image voxel	Ω_{vox}	2.3×10^{-3}	%
	Double detection efficiency for 511 keV	ϵ_{scint}^2	68 (2 cm), 86 (3 cm depth)	%
	Double photoelectric effect fraction	ϵ_{ph}^2	32 (LSO)	%

^aEnergy window: 400 - 600 keV ^bTypical for fractionated, carbon ion tumor treatments

The RTR dependence on the activity density of the object being imaged is plotted in Fig. 5.19 for LSO, LYSO with 50 % yttrium in respect to lutetium (elemental abundance) and LGSO

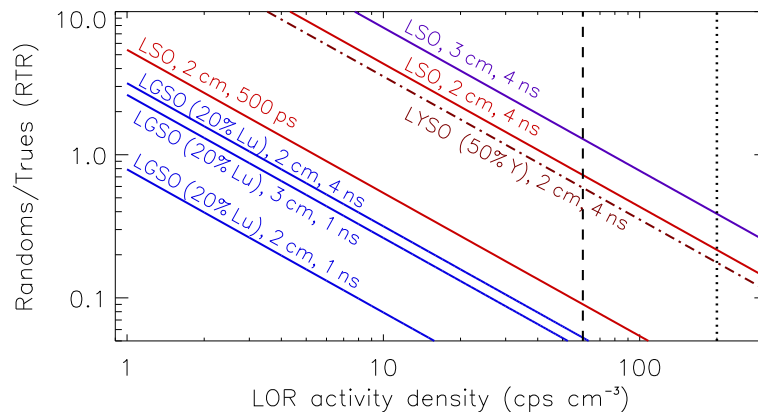


Figure 5.19: Randoms-to-trues-ratio RTR versus activity density in the object. Calculations were performed for one LOR formed by three different lutetium-based scintillators. For LSO the parameters of Table 5.4 were followed. The physical properties of LYSO and LGSO were taken from Table 4.1. The dashed and dotted vertical lines show the typical activity density for a dose maximum of 0.3 and 1 Gy, respectively, delivered with fractionated, carbon ion tumor treatments.

with 20 % lutetium in respect to gadolinium. By considering the maximum dose delivered at fractionated carbon ion tumor treatments, lying between 0.3 and 1 Gy, and a typical activity density per maximum dose unit of $200 \text{ Bq cm}^{-3} \text{ Gy}^{-1}$, a minimum and maximum activity density of 60 and 200 Bq cm^{-3} are obtained and are shown in Fig. 5.19 with a vertical, dashed and vertical, dotted line, respectively. These lines delimit, therefore, the region of interest to analyze for fractionated, carbon ion tumor treatments¹.

The analysis of Fig. 5.19 allows to see that an RTR close to unity is expected for low dose portals if LSO crystals with radial depth of 2 cm, or greater, and a coincidence time resolution of 4 ns are implemented. If the time resolution obtained with the detectors is decreased by about one order of magnitude, down to 500 ps, than Fig. 5.19 shows that the maximum RTR expected does not exceed 0.1. A coincidence time resolution of 500 ps is expected with LSO/APDA detectors under development² for PEM [San04], and has been measured [Ver05] by applying digital signal processing techniques to the timing signals of one pixel of the LSO/APDA detectors described in chapter 4. If the tomograph consists of crystals of LGSO with 2 cm radial depth, the maximum RTR expected reduces to approximately 5 %.

A value of $\text{RTR} = 1$ means that the PET signal is immersed in an activity background with the same intensity. The effects onto in-beam PET images of an $\text{RTR} = 1$ and $\text{RTR} = 0.1$ scenarios were simulated for the head and neck treatment studied in section 2.6.1, with the results displayed in Figs. 5.20 and 5.21, respectively. Table 5.5 shows the simulation details regarding the statistics considered for two tomographs, with $\phi = 0^\circ$ and $\phi = 46^\circ$ denoting a closed ring and a dual head tomograph (Fig. 2.1), respectively.

Table 5.5: Simulation of in-beam PET imaging with intrinsic detector activity (Fig. 5.20).

Randoms-to-trues ratio RTR	~ 1.0		~ 0.1	
Tomograph geometry	$\phi = 0^\circ$	$\phi = 46^\circ$	$\phi = 0^\circ$	$\phi = 46^\circ$
Total extrinsic true events simulated ($\times 10^6$)	2.5	2.5	2.5	2.5
Target volume (dm^3)	1.3	1.3	1.3	1.3
Average event density ($\times 10^6 \text{ events dm}^{-3}$)	1.9	1.9	1.9	1.9
Total extrinsic true events detected ($\times 10^3$)	237	174	237	174
Total intrinsic randoms simulated ($\times 10^6$)	7.5	7.5	0.75	0.75
Volume of image space with randoms (dm^3)	4.1	4.1	4.1	4.1
Average randoms density ($\times 10^6 \text{ randoms dm}^{-3}$)	1.8	1.8	0.18	0.18
Total intrinsic randoms detected ($\times 10^3$)	815	544	81	54

The images in Figs. 5.20 and 5.21 can be directly compared with the background-free reconstructions shown in Fig. 2.11. This comparison allows to conclude that an $\text{RTR} = 1$ scenario is clearly unacceptable since the positron annihilation signal is immersed in a sea of activity which disturbs image evaluation. This observation compromises the application of LSO-based detectors for in-beam PET (Fig. 5.19) if a coincidence time resolution at the nanosecond scale is applied. Nevertheless, the application of modern readout schemes allowing digital signal processing techniques to be implemented has proven to be able to lower the coincidence time resolution obtained with conventional nuclear electronics. Such techniques are mandatory for future, LSO-based, in-beam PET readout schemes since only a coincidence time resolution of 500 ps yields an acceptable RTR of 0.1 (Fig. 5.21). An alternative to reduce the background activity from the scintillator is to make use of recently available LGSO crystals [Shi04], containing

¹ For the same dose, a higher signal activity is expected for ion species with lower atomic number than ^{12}C due to their lower stopping power.

² This 500 ps coincidence time resolution will be achieved within the PEM project by means of digital pulse processing and with a double scintillation light readout per crystal [Lec02], with crystals of 20 cm depth.

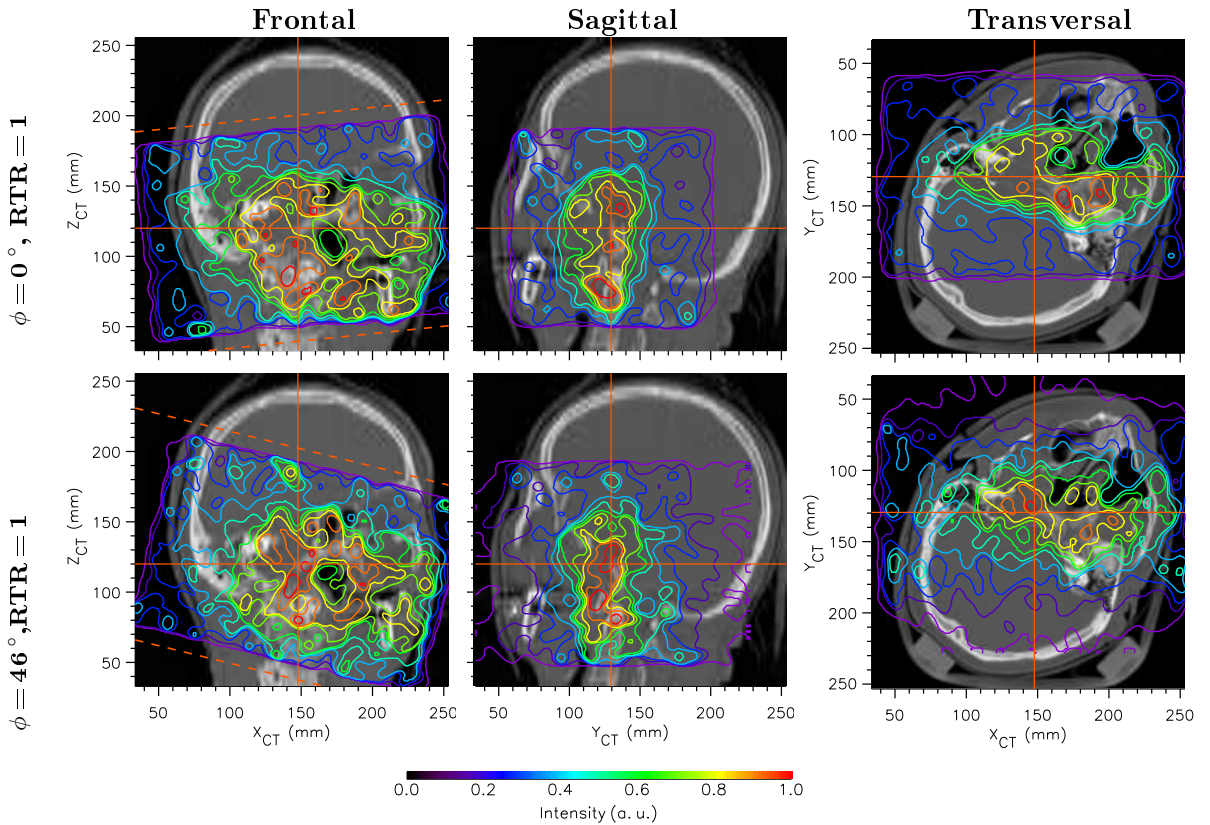


Figure 5.20: Influence of a high LSO background activity ($RTR = 1$) onto reconstructed images of a head and neck simulated treatment. The dashed lines in the frontal views show the limits (top view) of the dual-head tomograph considered.

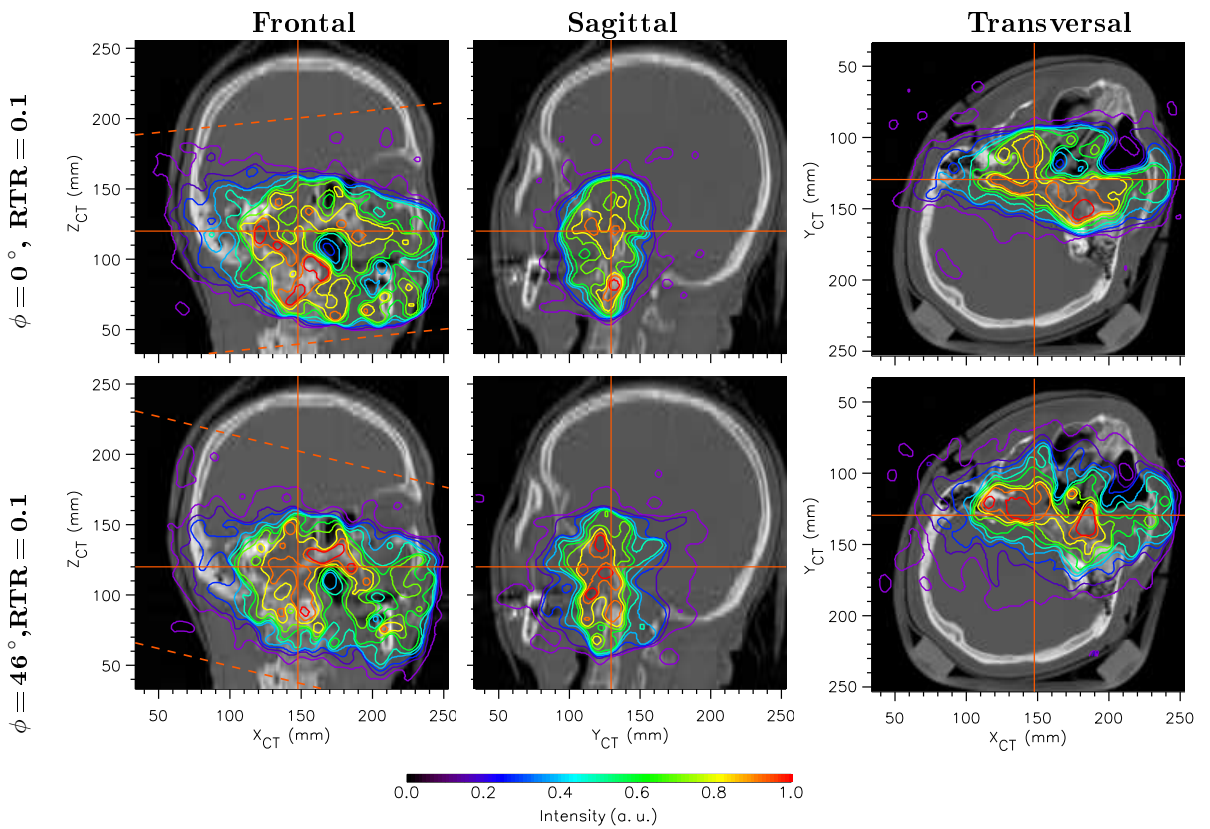


Figure 5.21: Influence of a low LSO background activity ($RTR = 0.1$) onto reconstructed images of a head and neck simulated treatment. The dashed lines in the frontal views show the limits (top view) of the dual-head tomograph considered.

80 % less lutetium but providing less detection efficiency than LSO, as shown in Table 5.6.

Table 5.6: Coincidence detection efficiencies^a (%) of several modern scintillators.

Scintillator	BGO	LSO	LGSO	GSO	LaBr ₃
2 cm radial depth	11.9	7.0	4.0	3.6	0.6
3 cm radial depth	14.4	8.8	5.4	4.8	1.0

^aOnly double photoelectric events are considered.

Influence of the intrinsic true rate T_i

As illustrated in Fig. 5.18, not only R_i contributes to the background measured in the total true coincidence rate T . The intrinsic true rate T_i , arising from events where a ¹⁷⁶Lu nuclide undergoes β^- -decay in one detector and emits a prompt γ -ray that is absorbed in a second detector, also contributes to the background measured. In order to estimate T_i , a blank scan performed with the ACCEL LSO-based tomograph [Wat04], yielding $T_i = 600$ cps measured with an energy window of 350-650 keV, was extrapolated to the dual-head tomograph with small gaps depicted in Fig. 5.1. This extrapolation takes into account the different volumes of the tomographs only and yields $T_i = 750$ cps and $T_i = 1134$ cps for 20 and 30 mm crystal depths, respectively. The obtained values were then normalized to the mid-plane between the detector heads and further attenuated by 46 % due to the presence of the patient¹ in the FOV of the tomograph [Lau00]. In the same publication the ratio of the intrinsic-to-extrinsic true coincidences, T_i/T_e , was estimated to be about 3.3 % for a narrower energy window of 400-600 keV and for a crystal depth of 20 mm [Lau00].

The value of T_i per unit area can now be directly compared with the extrinsic true coincidence rate T_e per unit area expected for this tomograph when imaging tumor treatments with carbon ion irradiation. For that, the average size of all clinical in-beam PET images acquired with BASTEI during carbon ion irradiation up to this date was considered: $22.3 \times 14.0 \times 15.1$ cm³. To this volume corresponds an area in the midplane between the two detector heads of about 312 cm². By taking into account a detection efficiency of approximately 4 % for BASTEI at the isocenter versus the 10 % covered also at the isocenter with the dual-head tomograph in Fig. 5.1, the typical 100 cps event rate measured with BASTEI scales up to 250 cps if a crystal depth of 20 mm is assumed. This corresponds to an expected signal activity density T_e normalized to the mid-plane between the detector heads of 0.8 cps cm⁻², which increases to 1.0 cps cm⁻² if the LSO crystal depth is extended to 30 mm. The values estimated are

Table 5.7: True coincidence rates due to the natural background from LSO. A dual-head tomograph with 90 cm diameter, 30 cm axial length, 2 or 3 cm radial depth and an opening angle of about 40° (Fig. 5.1) was considered in the calculations.

Energy window	400 - 600 keV		350 - 650 keV	
	20 mm	30 mm	20 mm	30 mm
Intrinsic true coincidences T_i (cps)	-	-	750	1134
in mid-plane (cps cm ⁻²)	-	-	0.30	0.45
attenuated (cps cm ⁻²)	-	-	0.14	0.21
Extrinsic true rate T_e^a				
in mid-plane (cps cm ⁻²)	-	-	0.8	1.0
T_i/T_e (%)	3.3 ^b	≥ 3.3	17.5	26

^aExtrapolated from BASTEI, energy window 250-850 keV

^bFrom [Lau00]

¹ Calculated for head and neck treatments only. Pelvis treatments yield a larger number of attenuated photons and, therefore, a further reduced T_i .

shown in Table 5.7. Its analysis allows to conclude that, as with the intrinsic randoms rate R_i , a better ratio of the intrinsic-to-extrinsic true coincidences, T_i/T_e , is obtained with a crystal depth of 20 mm if an energy window of 350-650 keV is considered. This ratio amounts to 17.5%, which is a background value to be added to the RTR ratio. Although an estimation of T_i can be made by performing a blank scan and computing the photon attenuation on the basis of the patient CT, the noise inherent to very low statistics data sets is difficult to remove. Therefore, a minimum energy window of 400-600 keV is an important condition to take into account for a lutetium-based tomograph imaging low intensity β^+ -activity distributions.

In summary, the best in-beam PET performance with LSO/APDA detectors is expected with an energy window smaller or equal to 400-600 keV and with a coincidence time resolution of 500 ps. An undesirable RTR close to unity is expected if lower dose portals are imaged with LSO crystals with a radial depth of 20 mm and 4 ns coincidence time resolution. This fact has been confirmed experimentally in [Cre05c]. Although random correction can be applied online to yield true counts in high-statistics human PET applications [Boe03], the low statistics sets of in-beam PET result in high variations of T_e and R_i due to noise, which may yield unsatisfactory random suppression. More importantly, recent accelerator developments to be implemented at future heavy ion therapy units, e.g. in Heidelberg, will compress the treatment duration by decreasing the time windows between beam extractions. The random suppression solutions described in chapter 6, allowing in-beam PET data taking during particle extractions, are not suited for subtracting an activity background stationary in time. In other words, the intrinsic true coincidence rate T_i arising from the natural background activity of LSO was estimated in [Lau00] to be about 3.3% of the in-beam PET signal¹, which does not influence significantly in-beam PET images acquired with BASTEI. This fact is confirmed for a next-generation, closed ring or dual-head tomograph but, the impossibility of efficiently suppressing the intrinsic random coincidences R_i suggests that digital signal processing techniques [Lec02, Ver05], decreasing the coincidence time resolution to 500 ps, are a main requisite for an LSO-based, in-beam PET tomograph. A modern, fast, high light-yield, radiation hard scintillator [Tan98] like LGSO [Shi04], containing 80% less lutetium than LSO, is also a choice if conventional nuclear electronics are to be used. With slightly higher detection efficiency² (ϵ_{det}^2) in respect to GSO (Table 5.6), a lutetium-free scintillator, the eventual choice of LGSO relies on its two times larger light yield (Table 4.1), which is an important factor for achieving optimum timing. This, in turn, is an important parameter in order to apply random suppression during particle extraction, as described in chapter 6.

5.7 Time-of-Flight for In-Beam PET

Recent developments have resulted in scintillators with high light yield and very fast fluorescence time constant. Best examples, shown in Table 4.1, are lanthanum bromide, LaBr_3 , and the very recently discovered cerium bromide, CeBr_3 , with light yields twice that of LSO and decay times of 35 and 17 ns, respectively. Together with LSO, these scintillators offer the possibility of using the time difference between the moment of detection of the two opposed γ -rays. This so-called time-of-flight (TOF) difference allows to restrict the location of the positron annihilation point within the LOR formed by the two hit detectors, as shown in section 5.7.1. For LSO-based detectors, it has long been foreseen that improvements in the readout electronics that could lead to a coincidence time resolution of 500 ps FWHM would reduce the noise variance in conventional PET imaging by a factor of 5 [Mos99a], i.e. for the same image quality the scan time may be 5 times shorter. Recently, a coincidence time resolution of 165 ps

¹ With an energy window of 400-600 keV and a scintillator depth of 20 mm.

² For a given tomograph, the scintillator-dependent ϵ_{det}^2 is multiplied by the scintillator-independent coincidence solid angle Ω_{coinc} in order to obtain the total coincidence detection efficiency.

FWHM has been measured between LaBr_3 and BaF_2 crystals, which can be extrapolated down to 73 ps FWHM if two LaBr_3 are used [Glo04]. Nevertheless, a slightly higher value of 313 ps FWHM has been reported [Kuh04a] between two LaBr_3 -based detectors with an Anger-logic-based readout scheme [Kuh04b], i.e. with the reduced electronics channels typically installed in commercial PET scanners. These values could be reduced if a data readout allowing digital signal processing techniques to be applied would be implemented, as verified with LSO-based detectors [Var05, Ver05].

With the current trend in the coincidence time resolution of PET detectors pointing towards hundreds or even tens of picoseconds, it seems to be reasonable to analyze the impact of such developments for in-beam PET. In addition to reduce the noise background of PET images, TOF techniques gain much importance for dual-head, in-beam PET scanners due to the capability of the TOF information to reduce the longitudinal image elongation studied in chapter 2. Equally important, both for closed-ring as well as for dual-head, in-beam positron tomographs, is the immense decrease in data processing time if the TOF information is used, making in-beam TOF-PET images available even during the irradiation for tomographs with a coincidence time resolution below 200 ps FWHM [Cre05a].

5.7.1 Principles of the time-of-flight technique

Fig. 5.22 illustrates the physics principle inherent to TOF-PET. If the detectors and readout electronics of a given PET scanner provide a coincidence time resolution below the nanosecond scale, then the time difference between the arrival of the photons to each detector may be used to restrict the location of the annihilation point within the LOR formed by the two detectors. For any given LOR formed by detectors a and b , the coordinate x which gives the distance from the center of the LOR to the point where the positron annihilated, is given by $x = (t_b - t_a) \cdot c / 2$, with c being the speed of light. The spatial resolution that can be obtained for x corresponds to half the coincidence time resolution between detectors a and b . Such mechanism reduces greatly the contribution of Compton scattered and random photons arriving from outside the FOV of a 3D tomograph, therefore enhancing the signal to noise ratio of TOF-PET images [Mos04]. This makes TOF-PET attractive when imaging large objects, as is the case of tracer imaging in conventional human PET.

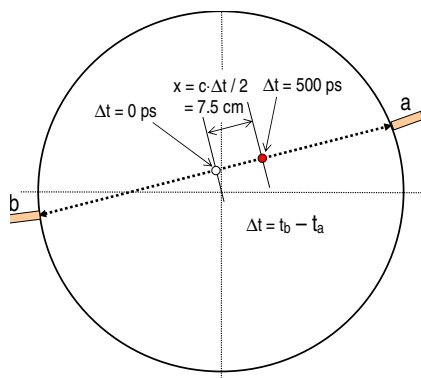


Figure 5.22: Principle of the time of flight technique in tomography. The color-filled circle depicts an annihilation located 7.5 cm from the middle of the LOR between two given detectors. This corresponds to a photon path difference of 15 cm. Therefore, the spatial resolution obtained with TOF-PET is half the coincidence time resolution of its detectors times the speed of light.